Small-scale dynamo in cool main-sequence stars

Dissertation

zur Erlangung des mathematisch-naturwissenschaftlichen Doktorgrades

"Doctor rerum naturalium"

der Georg-August-Universität Göttingen

im Promotionsstudiengang Physik

der Georg-August University School of Science (GAUSS)

vorgelegt von

Tanayveer Singh Bhatia

aus Ludhiana, Indien

Göttingen, 2022

Contents

Summary

Cool stars have an outer convection zone which can produce magnetic fields. In many main sequence stars, including the sun, the magnetic field has a large scale, cyclic component that is driven by a global dynamo and manifests as sunspots, active regions, CMEs and flares. There is also a quiet, cycle-independent component to these magnetic fields that is thought to account for a substantial amount of unsigned quiet-sun flux, making it important for basal chromospheric (and coronal) heating. This quiet component is observed as small-scale mixed polarity fields with stronger concentrations (network fields) outlining the boundaries of supergranular convection and weaker ones (internetwork fields) occupying the region within these boundaries. State of the art simulations seem to suggest that a small-scale dynamo (SSD) is, at least partially, responsible for the quiet sun magnetic fields. In an SSD, magnetic fields are amplified by the small-scale turbulent motions of the plasma in the convection zone. Simulations indicate that an SSD is expected to operate throughout the convection zone, and is not necessarily limited to the near-surface convection. SSD driven magnetism has been investigated thoroughly for the solar case, but its effect on models atmospheres of other cool main sequence stars remains yet to be explored.

Model atmospheres are essential for interpreting stellar observations and extracting fundamental stellar parameters like mass, age, surface gravity, metallicity and effective temperature. These models are usually constructed over a grid of effective temperature, metallicity and surface gravity, and the model spectra are fitted to the observed spectra to extract stellar parameters. Better models allow better constraints, not only on our understanding of stellar evolution, but also detection and characterization of exoplanets and determination of stellar abundances. However, most such grids (e.g, ATLAS, PHOENIX and MARCS) that have been widely used are based on 1D atmospheres, which employ an approximate phenomenological treatment of convection. This requires using free parameters like mixing length and microturbulence and do not accurately model the effect of realistic convection on spectral line profiles. Recently, grids of 3D stellar atmospheres with realistic convection have been constructed (CIFIST, STAGGER), which, in hand with increasingly accurate observational missions (Kepler/K2, TESS, Gaia, PLATO etc.) allow even more precise determination of stellar parameters and exoplanet characterization. These models, however, are purely hydrodynamic. In order to further improve them, we must take into account affect of SSD fields.

This thesis is a starting point in the construction of a grid of atmospheres for cool main sequence stars over a range of effective temperatures, surface gravities and metallicities. We start off with four stellar atmospheres, an F3V, a G2V, a K0V, and an M0V star, with an SSD mechanism generating magnetic fields. We then compare the SSD runs against respective purely hydrodynamic runs to see what changes between the two. The

SSD mechanism generates magnetic fields for all cases with energy within an order of magnitude of the kinetic energy. The energy required for the magnetic fields essentially comes from the kinetic plasma motions, resulting in a decrease in convective velocities and, accordingly, turbulent pressure. The amplitude of differences between the SSD and the hydrodynamic cases scale directly with effective temperatures. For the F-star, where convective velocities can easily become supersonic, this effect is strong enough to slightly change the near surface thermodynamic stratification. In the photosphere, the SSD fields show a remarkably similar distribution for all the stars and the presence of kilogauss field concentrations in intergranular lanes is well-correlated with formation of bright points. This effect is not as strong for the M-star as it is for the other cases. In terms of possible observational signatures, a very simple estimation of a proxy convective blueshift indicates a significant reduction in expected convective blueshift for the hotter stars, necessitating computation of synthetic spectra to study affects of SSD magnetism on limb darkening, spectral line shifts and stellar variability as next steps.

1 Introduction

1.1 Observing stellar magnetic fields

Magnetic fields play an important role in almost all stages of a star's life. During star formation, they help transport angular momentum radially outwards, which affects, among other things, planet formation. This continues to take place throughout the main-sequence stage via a magnetized stellar wind. During this phase, magnetic fields are continuously generated in stars due to some sort of dynamo action. As the star approaches the end of its fusion lifetime, it loses its outer layers, either in form of a planetary nebulae or, if the star is massive enough, a supernova. What's left behind is a compact object like a white dwarf (in the former case) or a neutron star or even a black hole (in the case of the heaviest stars). Here, the magnetic fields continue to play a role, either as strongly compressed fields from the original star (Koester and Chanmugam 1990) or as intense fields generated from rapid dynamo action (Duncan and Thompson 1992). Pulsars, that is, magnetized rotating neutron stars, function as extremely precise cosmological clocks with applications ranging from tests of general relativity to possible interstellar navigation. They also provide a conduit for impressive jets associated with black holes (Blandford and Znajek 1977), and could possibly influence the masses of the heaviest white dwarfs (Das and Mukhopadhyay 2013).

Before we get to observations of stellar magnetism, it is important to understand how magnetism manifests in observations of the sun. The solar atmosphere consists essentially of three layers: the **photosphere**, which is visible to the naked eye (hence 'photo') and where the mode of energy transfer changes from convective to radiative; the **chromosphere**, the layer right above the photosphere which is visible during solar eclipses as a deep red ring (which gives this layer its name) due to emission from an atomic hydrogen line called Hα; and the **corona**, a hazy ring extending outwards, visible to the naked eye during a solar eclipse. The sun's magnetic fields are associated most obviously with dark photospheric features like sunspots, and bright photospheric features like faculae (from the Latin word for 'little torches'). In the chromosphere, the magnetic fields produce bright plages (from the French word for 'beach'). The corona itself is much hotter than the photosphere and the chromosphere and the heating mechanism is believed to be connected to the magnetic activity in the lower layers. Magnetically active regions on the solar surface are associated with coronal loops and holes, giving the corona its structure. When the sun rotates, these features move across the surface, resulting in variations of spatially-averaged intensity. The (differential) rotation, combined with convection of plasma in the solar interior, is expected to give rise to a dynamo process (Parker 1955, Babcock 1961). A dynamo draws energy from the kinetic motions and amplifies and

sustains magnetic fields against dissipation due to resistivity. On the sun, a global dynamo results in the solar magnetic cycle, where the global magnetic fields flip roughly every 11 years. This cycle is visible not only in the number of sunspots, but also chromospheric activity as measured through Ca II H&K emission lines[1]. In fact, most of the cycle-dependent magnetic activity is associated with this global dynamo process. There is also a quiet, cycle-independent component to this activity, termed quiet sun magnetism, the details of which are discussed in Sect. 1.3.

We expect most cool sun-like[2] stars to have magnetic fields with observational signatures analogous to what we see on the sun. The evidence for this comes from observations of photometric and chromospheric variability. Intrinsic photometric variability is expected to be the result of starspots and faculae-like bright features moving across the stellar surface. In fact, the assumption that spots on sun-like stars behave similarly to the sun allows us to estimate rotation rate without the ambiguity of viewing angle inherent in estimating rotation rates from Doppler broadening of spectral lines (Radick et al. 1987). Measurements of stellar chromospheric activity using Ca II H&K emission lines has been important for establishing a connection between stellar ages and rotation-rate (Skumanich 1972) and providing an independent way of estimating ages for sun-like stars (Barnes 2003). The Ca II H&K emission intensity is related to the magnetic field strength. This field is assumed to be generated by a dynamo whose strength is dependent on the rotation rate. As stars age, their rotation rate decreases due to angular momentum loss by outflowing plasma termed stellar wind[3]. If this wind is magnetized, it is forced to co-rotate with the star up to some critical distance, which causes the star's angular momentum to decrease faster than expected compared to a simple thermal wind (Schatzman 1962, Mestel 1968). This decreased rotation rate decreases the efficiency of the global dynamo, which decreases the global magnetic field strength and, accordingly, the Ca II H&K emission intensity. Long-term observations of stellar chromospheric activity (Wilson 1978, Baliunas et al. 1995) indicate the existence of cyclic behavior of magnetic activity on other cool sun-like stars and have been essential in extending our understanding of stellar dynamos. In addition, magnetic fields can broaden spectral lines due to Zeeman splitting of atomic levels and induce polarization. Signatures of these effects in stellar spectra give a more direct indication of magnetic fields. In practice, the technique usually used to directly measure stellar magnetic fields is called Zeeman-Doppler imaging (Semel 1989, Donati et al. 1997). Here, the principle is that the surface of a rotating star can be divided into bands based on regions of similar line-of-sight velocities, with the bands near the edge (limb) having higher velocities due to rotation than those near the center. If a starspot appears, the magnetic field will modify the spectral line shapes. Depending on which velocity band it appears in, this change in spectral line profiles will be Doppler shifted by some amount. This allows a way to map starspots on the stellar surface. More recently, interferometry has made it possible for a few giant stars to be directly resolved, allowing observations of spatial variations in intensity (Roettenbacher et al. 2016).

Understanding the origin and evolution of the magnetic fields throughout a star's his-

---

[1]Here 'II' refers to the first ionized state of calcium and H and K refer to the terminology used by Fraunhofer in his description of the solar spectrum

[2]sun-like stars refers to stars with an outer convection zone and mass similar to the mass of the sun. See 1.2 for a detailed description.

[3]The existence of such a wind for the sun was first theoretically described by Parker (1958).
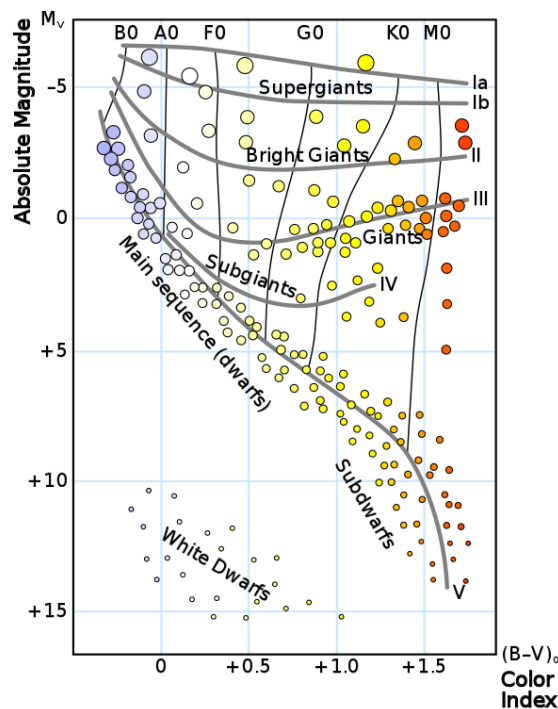
Figure 1.1: Schematic Hertzsprung-Russell diagram showing the various stellar populations as a function of absolute magnitude M_V (y) and B-V color (x). Credit: Rursus, CC BY-SA 3.0 `http://creativecommons.org/licenses/by-sa/3.0/`, via Wikimedia Commons

tory would improve our understanding of stellar structure and evolution. There are a number of excellent reviews that cover observational evidence of stellar magnetism (Reiners 2012) and its connection to solar-magnetism, dynamo theory, etc. (Brun and Browning 2017, Donati and Landstreet 2009). Here, we limit ourselves to partly understanding the role magnetic fields generated at small scales play in sun-like stars during a relatively quiet but long phase of their lives: the main-sequence of the Hertzsprung-Russell (HR) diagram.

1.2   Understanding stellar spectra

The HR diagram (see Fig. 1.1 for a schematic representation) is a scatter plot of stellar brightness/absolute magnitude (or luminosity) against color (or, equivalently, effective temperature[4]). Each point represents a star with a particular brightness and color. The distribution of stars on the HR diagram directly led to a deeper understanding of stellar evolution, the prediction of nuclear fusion as a source of stellar luminosity, the recognition of the importance of radiation pressure in stellar structure and the development of mass-luminosity relations (Eddington 1926). Most stars lie in a dense region extending

---

[4]Effective temperate corresponds to the temperature obtained from assuming the star emits radiation like a blackbody at a specific temperature and fitting the star's observed spectral profile to the expected blackbody spectral profile.

from top left to bottom right. This is called the main-sequence. It corresponds to the longest evolutionary stage that a star experiences. The diagram is usually divided into spectral classes based on the Morgan-Keenan system in the horizontal direction (going from hottest to coldest: O, B, A, F, G, K, M) and in luminosity classes in the vertical direction (going from brightest to dullest: 0, I - supergiants, II - bright giants, III - giants, IV - subgiants, V - dwarfs/main-sequence, VI - sub dwarfs, VII - white dwarfs). The spectral classes are usually further subdivided from 0 (hottest) to 9 (coldest) for each class. The sun, accordingly is a G2V star, corresponding to an effective temperature of around 5800 K. All main-sequence stars have cores supported by nuclear fusion of hydrogen to helium and the stars ranging from F to M3 have an outer convection zone. Hotter stars have a convective inner core and an outer radiative zone while cooler stars are fully convective.

As the understanding of main-sequence stellar structure and evolution developed over time, it was realized that the major factors that influence where a star ends up on the HR diagram are its age, initial mass (before the beginning of nuclear fusion) and metallicity (that is, the fraction of elements heavier than hydrogen and helium). Assuming spherical symmetry, the equations of stellar structure and evolution can be written down in a relatively straightforward manner (see chapter 10 of Kippenhahn et al. (2013) for a list of equations). The devil is in the details, and a description of what goes into the solution is beyond the scope of this thesis. What's important is that these equations allow the computation of model stellar atmospheres and corresponding spectra (Kurucz 1979, Gustafsson et al. 2008). For computing the spectra, effective temperature, surface gravity and metallicity are supplied as input. The spectra computed over a range of these three parameters can then be compared to to real spectra and the best fit is then used to characterize a star. For an example of the methods involved, see Sneden (1973). This is important for determining elemental abundances, which leave their signature in the spectra, as well as for understanding how transiting exoplanets might affect the observed spectra.

As mentioned, the most widely used model atmospheres are 1D. This implies a phenomenological model of convective energy transport. This is usually done via some form of mixing length theory (MLT) (Böhm-Vitense 1958), where the mixing length refers to the effective height over which a parcel of plasma rises before losing its identity and mixing with the background. This height is assumed to be proportional to the local pressure scale height, with the constant of proportionality α_{MLT} being a free parameter. For computing spectra, this is not a very good approximation (Kurucz 1996). Since convection is inherently a 3D process with hot upflows and cool downflows, these models fail to account for potential affects of the 3D nature of convection on spectral synthesis. These models also do not account for the effect of magnetic fields on the generated spectra (Babcock 1947, Reiners 2012).

1.3   Quiet sun magnetism and small-scale dynamo

As mentioned in the Sect. 1.1, magnetic activity in the sun is understood to be due to some form of dynamo operating in the convective envelope, resulting in features like sunspots, flares, coronal loops, prominences, faculae etc. However, the solar magnetic field also has a quiet part, termed appropriately as quiet sun magnetism. Quiet sun magnetic fields are usually divided in two classes: network and internetwork fields. Network fields are
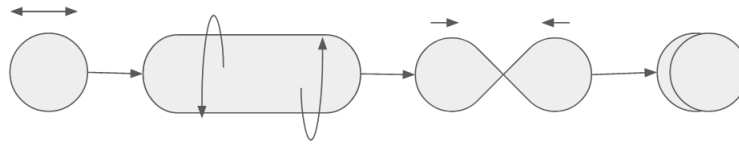
Figure 1.2: Illustration of the stretch-twist-fold mechanism: the magnetic loop gets stretched by the plasma motions, then twisted and doubled on itself.

strong (in the kilogauss regime) and outline the largest scales of surface convection, called supergranulation. Internetwork fields are weak (hundreds of gauss) and occupy smaller scales. These fields are largely independent of the magnetic cycle (Buehler et al. 2013) and their contribution to the total magnetic flux is comparable to that of active regions (see Bellot Rubio and Orozco Suárez (2019) for an overview). In other stars with a convective envelope, we use the term quiet star magnetism. This will be the main focus of this thesis. Before going on to the implications of the magnetic field in other stars, let's try to understand how it arises on the sun and the theoretical basis for the processes involved.

Any magnetic field in plasma will dissipate over time due to magnetic resistivity. To combat that, one requires a dynamo mechanism (the idea behind a dynamo is described in section 1.1). The quiet sun magnetism must at least partially be attributed to a dynamo mechanism independent of the large scale dynamo, and operate at "small" spatial and temporal scales, compared to the size of the convection zone and the scales at which the curvature and rotation of the sun become important. Petrovay and Szakaly (1993) showed using a transport model for magnetic fields that the observed strength of small-scale fields requires a source term with a small time-scale for replenishing the field against dissipation. They attributed this to a small-scale dynamo (SSD) operating in the convection zone. Numerous turbulent plasma simulations seem to result in amplification of fields via an SSD mechanism (Schekochihin et al. 2004b, Moll et al. 2011). An intuitive picture of the amplification process can be understood as a stretching-twisting-folding mechanism caused due to turbulent plasma motions. Weak magnetic fields are dragged along with the plasma (as magnetic flux is conserved in ideal MHD equations) and stretched, twisted and folded back, and (with a little bit of magnetic resistivity) merged together. This increases the magnetic flux across a given cross-section (see Fig. 1.2 for a schematic). More rigorously, theoretical groundwork for a dynamo action supported by turbulent plasma had already been laid by Kraichnan and Nagarajan (1967) and Kazantsev (1968), who showed analytically that a kinematic (that is, magnetic field is influenced by plasma velocity but not vice versa) dynamo is possible in an idealized turbulent system. However, if the velocity field is more realistic/complicated and the magnetic field becomes strong enough to influence the plasma, things become more complicated, and numerical simulations are required.

Turbulence is an infamously hard problem to study, even if one does not include magnetic fields. As a starting point, a fluid with some scale length L, a characteristic velocity U and viscosity ν can be characterized in terms of the dimensionless Reynolds number $Re = UL/\nu$. The higher this number is, the more turbulent the fluid is likely to be. When magnetic fields are present and the fluid has some magnetic resistivity η, an equivalent magnetic Reynolds number can also be defined as $Rm = UL/\eta$. Looking at the

spatial power spectra (that is, a plot showing a distribution of power contained at each scale length) of the kinetic and magnetic energy of such a fluid gives an idea of the scale at which power is injected into the system and the scale it ultimately gets dissipated at. For any dynamo mechanism, there exists a competition between dissipation and amplification of the magnetic fields. Because of this, there exists a critical value of magnetic Reynolds number Rm_c below which dynamo action ceases. Since Rm_c depends on the scales and velocities of the system under consideration, an important parameter to consider is the magnetic Prandtl number ($Pm = Rm/Re = \nu/\eta$), which is an intrinsic property of the plasma itself. For a turbulent plasma system with large Pm, magnetic fields exist as smooth and highly stretched and folded structures. A small Pm corresponds to a system with rough velocity field and irregular and finely structured magnetic field at the smallest scales. For an illustration, see Fig. 16 of Rincon (2019). Most astrophysical systems have either a very large (galactic plasma) or a very small Pm (stellar convection). In the solar convection zone, estimates for Pm range from 10^{-2} for the base of the convection zone to 10^{-6} in the photosphere. Hence, some numerical simulations trying to understand the role of an SSD in the sun have tried to model this low-Pm regime (Iskakov et al. 2007, Schekochihin et al. 2004a). However, the real ranges are not yet accessible to current simulations. The studies mentioned here try to approach this regime asymptotically. It seems that when Pm < 1, the SSD is not as easy to excite as for Pm >> 1. Most recent high-resolution simulations seem to show that it might be possible to excite at low-Pm, and that it becomes progressively easier to do so (Warnecke et al. 2022) at Pm < 0.05, with the roughness of velocity field (Falkovich 1994) being responsible for the difficulty in exciting a dynamo in the range 0.05 < Pm < 1. For a review of astrophysical dynamos, see Brandenburg and Subramanian (2005a). Simulations of solar convection (Cattaneo 1999, Bercik et al. 2005) with a stratified background, and with increasingly realistic setup (Vögler and Schüssler 2007) showed that an SSD could maintain a significant amount of magnetic field in the solar photosphere.

Observations of quiet-sun field based on Hanle-effect diagnostics (Trujillo Bueno et al. 2004), estimate the quiet-sun magnetic field to be ~ 130 G. The Hanle-effect refers to the change in the plane of polarization of light when there is a weak magnetic field present perpendicular to the line of sight. The energy levels of the plasma atoms that scatter the light (in some typical time τ_s) are affected by this magnetic field. In the classical picture, the weak field causes Zeeman splitting of degenerate energy levels and induces Larmor precession of the angular momentum axes. This manifests as a rotation with some timescale τ_r of the plane of polarization. The timescale τ_r is dependent on the strength of the magnetic field. If $\tau_r \sim \tau_s$, it results in a decrease in the amplitude of polarization, i.e. depolarization, in the line-of-sight (see Trujillo Bueno (2001) for a more complete explanation). Early realistic solar convection simulations with SSD (Vögler and Schüssler 2007, Danilovic et al. 2010) found that SSD fields were lower by a factor of 2 to 3 compared to the observed Hinode/SP flux densities. Rempel (2014) studied the effect of resolution, diffusivities and bottom boundary on the photospheric field strength. He found the field distributions to be robust, the field strength to converge towards observationally inferred values to within a factor of 1.5, with increasing resolution and an open bottom boundary (to mimic deeper convection). Accordingly, fields associated with an SSD are expected to contribute significantly to the quiet sun field.

Lastly, recent high resolution simulations have pointed to the possibility that solar

differential rotation might be related to field generated from an SSD (Hotta et al. 2022), with the meridional flow responsible for a fast equator being maintained by the Maxwell stresses from the SSD fields. Hence, it is important to consider the potential effects of SSD fields on stellar observations.

1.4   Quiet star fields

With the advent of high precision exoplanet detection, it is important to understand the effect stellar magnetism might have on the light curves of stars with exoplanets. The two major methods of detecting exoplanets are transit photometry and radial velocity (RV)/Doppler spectroscopy. In transit photometry, whenever an exoplanet transits its host star, part of the lightcurve is blocked. By studying this dimming, the size of the candidate exoplanet can be determined. The *Kepler*/K2 NASA satellite mission essentially ushered in an new era of exoplanet detection via precise wide-field transit surveys (Borucki et al. 2010, Howell et al. 2014), paving the way for further, more ambitious missions including NASA's TESS (Ricker et al. 2014) and ESA's PLATO (Rauer et al. 2014). However, just by itself, this method only provides the minimum mass of a planet due to viewing angle dependence, and is prone to a high rate of false detections. This is because variability of stellar lightcurves is influenced by a variety of factors, including stellar magnetism. This can be mitigated to a significant degree by employing the RV method. Exoplanets can make their host star 'wobble' due to their own gravitational force. Because of the orbiting motion, this results in a characteristic Doppler shift in spectral lines. Measuring and characterising the properties of an exoplanet based on this shift is the basis of the RV method. Before the *Kepler* mission, the HARPS spectrograph (Mayor et al. 2003, Pepe et al. 2004) was the most successful exoplanet-finder. When coupled with transit photometry for targeted observations of exoplanet candidates, RV is an extremely powerful method for characterization of potential exoplanet candidates. However, for detection of rocky exoplanets with modern high-resolution spectrographs like ESPRESSO (Pepe et al. 2021), the precision needed requires a deeper understanding of stellar variability and the factors that affect it, including magnetic fields. For a comprehensive list of factors affecting RV measurements, see Table A-4 in Crass et al. (2021). Better stellar models would help distinguish between, e.g., a spot moving across the surface of a star vs. a transiting exoplanet. In the context of other stars, the SSD-associated quiet star magnetism could be expected to influence pressure oscillation frequencies as well as reduce the convective blueshift (that is, the average blueshift in spectral lines because of outflows occupying a larger fraction of the stellar surface compared to downflows) in photospheric spectral lines. (Shporer and Brown 2011) showed that convective blueshift can be important for correctly interpreting the RV curves for a transiting exoplanet.

The reduction in convective velocities due to SSD fields may have implications for stellar structures and differential rotation, as Hotta et al. (2022) showed in their global simulations. SSD fields would also constrain the basal magnetic flux, which could influence chromospheric activity and its interpretation. In addition, it may also influence granulation flicker, which is an additional empirical method (along with astroseismology) of determining stellar parameters (Bastien et al. 2013). Last, but not the least, detailed realistic simulations also allow precise determination of stellar abundances, which could

have implications for stellar structure and evolution. Asplund et al. (2009, 2021) showed the importance of determining these abundances accurately for the sun, as these serve as a yardstick for cosmological distance measurements as well as for understanding the discrepancy between abundance measurements with helioseismology against 3D simulations, with implications for validity of widely used stellar models.

1.5   This thesis

The need to develop 3D MHD models that incorporate SSD fields becomes apparent with the context presented in the previous subsections. As mentioned before, estimating stellar parameters and abundances requires comparison with stellar models. This is done by comparing against a grid of atmospheres over different metallicities, effective temperatures and surface gravity (see Jofré et al. (2019) for a review of the steps involved). As 1D models start becoming insufficient for detailed comparison at the precision afforded by modern day instruments, especially at bluer/UV wavelengths, and to avoid dependence on free parameters like mixing length and microturbulent velocity, 3D models have become necessary. The most comprehensive such grids of models are the STAGGER (Magic et al. 2013) and the CO5BOLD (Freytag et al. 2012) grids. The STAGGER grid has been used to develop synthetic spectra (Chiavassa et al. 2018) which show small but significant deviations from 1D model spectra, especially in the line-crowded parts of the stellar spectra. These models are, however, purely hydrodynamic. With increasing precision of RV measurements, it's important to quantify the effects of stellar granulation properly, which could be influenced by quiet star magnetism. Recently, steps have been taken to understand the effect of unipolar magnetic fields of varying strengths on near-surface stellar structure and atmosphere (Beeck et al. 2015a, Salhab et al. 2018), but these are more analogous to active regions. This thesis studies the effect of quiet star magnetism in the context of an SSD, using 3D MHD models with self-consistently generated SSD magnetic fields. These are compared against reference hydrodynamic models to analyze changes in thermodynamic stratification, convection, intensity structure, photospheric velocities etc.

All the simulations here were done using the *MURaM* code. *MURaM* is a 3D radiation-MHD code that models near surface convection in a realistic manner (Vögler et al. 2005, Rempel 2014, 2017, Przybylski et al. 2022). The equations for mass, momentum and energy conservation, along with the induction equation for magnetic field are solved explicitly. The radiative transfer equation is solved by using short characteristics, with grey as well as multi-band binned opacities based on opacity distribution functions (ODFs). The actual equations and the the meaning of symbols used are covered in Sect. 2.2. The same section also covers the bottom boundary conditions which essentially fix the effective temperature, the height where the optical surface forms and the distribution of magnetic fields. The last mentioned aspect was explored in the solar context by Rempel (2014), where it was shown how having an open bottom boundary for magnetic fields is important for being consistent in mimicking deeper simulation boxes.

All analyses were done with Python, using Jupyter notebooks [5]. Extensive use was

---

[5]https://jupyter.org/

made of numpy[6] for data analysis and matplotlib[7] for making plots. Details for chapter-specific methods are contained in the appendices for each chapter.

[6]https://numpy.org/
[7]https://matplotlib.org/

2 Changes in stratification and near-surface convection for main-sequence stars

Abstract

Context: Some of the small-scale solar magnetic flux can be attributed to a small-scale dynamo (SSD) operating in the near-surface convection. The SSD fields have consequences for solar granular convection, basal flux, and chromospheric heating. A similar SSD mechanism is expected to be active in the near-surface convection of other cool main-sequence stars, but this has not been investigated thus far.

Aim: We aim to investigate changes in stratification and convection due to inclusion of SSD fields for F3V, G2V, K0V, and M0V spectral types in the near-surface convection.

Methods: We studied 3D magnetohydrodynamic (MHD) models of the four stellar boxes, covering the subsurface convection zone up to the lower photosphere in a small Cartesian box, based on the *MURaM* radiative-MHD simulation code. We compared the SSD runs against reference hydrodynamic runs.

Results: The SSD is found to efficiently produce magnetic field with energies ranging between 5% to 80% of the plasma kinetic energy at different depths. This ratio tends to be larger for larger T_{eff}. The relative change in density and gas pressure stratification for the deeper convective layers due to SSD magnetic fields is negligible, except for the F-star. For the F-star, there is a substantial reduction in convective velocities due to Lorentz force feedback from magnetic fields, which, in turn, reduces the turbulent pressure.

Conclusion: The SSD in near-surface convection for cool main-sequence stars introduces small but significant changes in thermodynamic stratification (especially for the F-star) due to a reduction in the convective velocities.

2.1 Introduction

The interpretation of data from stellar observations requires comparison against stellar models. Traditionally, these models have been 1D global models (Carbon and Gingerich

1969) that use formulations of mixing-length theory (MLT) (Böhm-Vitense 1958). Later models have accounted for line-blanketing effects and used an opacity distribution function (ODF) approach to calculate opacities (Strom and Kurucz 1966). Among them, the *MARCS* code (Gustafsson et al. 1975, 2008), the *ATLAS* code (Kurucz 1979, Castelli and Kurucz 2003), and the *PHOENIX* code (Allard and Hauschildt 1995, Hauschildt et al. 1999) have enabled the calculation of synthetic stellar spectra with a detailed accounting for the relevant physics. These models have enabled, for example, the accurate determination of abundances and stellar evolution tracks, along with constraining the chemical evolution of galaxies (Edvardsson et al. 1993).

Nonetheless, convection is a 3D process and a phenomenological 1D approach is insufficient for characterizing the properties of granulation and plasma turbulence. Radiative aspects of granulation, in particular, are not fully captured by an MLT-like approach. The 1D models also require free parameters, such as the mixing length parameter, α_{MLT}, and turbulent velocities for line broadening calculations. Hence, 3D stellar atmosphere models become important for a realistic interpretation of stellar characteristics from observations. The first 3D simulations of solar convection were pioneered by Nordlund (1982), Stein and Nordlund (1998), Nordlund and Stein (1990). These simulations are realistic in the sense that they are directly comparable to solar observations: they reproduce granulation pattern and associated spectral line widths and asymmetries quite well (Asplund et al. 2000).

Early stellar models (Nordlund and Dravins 1990) showed the limitations of MLT-based models in accurately reproducing the near-surface temperature gradient, which affects radiative properties in the lower photospheres. Subsequently, various models have been constructed over a grid of effective temperature, surface gravity, and metallicity. Currently, the most comprehensive 3D grids (Magic et al. 2013, Ludwig et al. 2009) cover a wide range of stellar type on the HR-diagram, but they are purely hydrodynamic.

However, stellar convection is not a purely hydrodynamic process. Most cool stars are expected to have magnetic fields. Hence, a complete description of their photospheres should also take into account the effects of such fields. The best studied star in this context is the Sun. There is a rich variety of solar magnetic field-related phenomena ranging from sunspots and active regions to network fields, forming plages and faculae all the way down to small-scale mixed polarity turbulent magnetic field filling the rest of the solar surface. State-of-the-art solar simulations reproduce all of these features, from sunspots (Rempel et al. 2009) and plages (Vögler et al. 2005, Yadav et al. 2021) to quiet-sun magnetism (Rempel 2014).

The quiet-sun small-scale field, that is, the field associated with regions of the sun not showing any activity, is partly attributable to a small-scale dynamo (SSD) operating in the convection zone (Vögler and Schüssler 2007, Rempel 2014, Pietarila Graham et al. 2010). This field is believed to have a significant magnitude of around ~ 130 G, based on Hanle depolarization (Trujillo Bueno et al. 2004). Additional evidence that a fair fraction of the small-scale field is a result of an SSD comes from the fact that internetwork magnetic flux does not follow the solar cycle (Buehler et al. 2013, Lites et al. 2014). In realistic radiative-MHD simulations, the effect of quiet-sun magnetic fields (self consistently generated via an SSD mechanism) has previously been shown to be important, for example, to reproduce the correct solar intensity contrast (Danilovic et al. 2010) and account for inferred photospheric magnetic field strength based on Hanle-effect diagnostics

(Shchukina and Trujillo Bueno 2011). In addition, there is a tendency to obtain a rough equipartition between kinetic and magnetic energy in SSD simulations (Hotta et al. 2015, Haugen et al. 2004, Schekochihin et al. 2004b), which implies a substantial reduction in plasma velocities since most of the energy in the magnetic fields is obtained from the plasma motions. The importance of magnetic fields generated from an SSD in other stellar types and its effect on the intensity characteristics, however, remains to be explored. Hence, it is imperative to investigate the effect of quiet-star small-scale magnetic fields on these quantities in a subsequent study.

This paper is a part of a project aimed at constructing a grid of magneto-convective stellar atmospheres, ranging across temperatures ($3500 < T < 7000$ K), gravity ($4.3 < \log_{10} g <$ 4.8 in cgs units), and metallicities (in this paper, only solar metallicities are considered). We investigate four stellar cases: F3V, G2V, K0V, and M0V and we study the relative change in stratification, convection, and intensity from purely hydrodynamic setups.

In §2.2, we outline the simulation code and the setup. Then, we present the results of the simulations in §2.3, followed by interpretation of the results in §2.4. Lastly, we summarize the results and present the corresponding discussion in §2.5.

2.2 Methods

2.2.1 Simulation code

The code we use throughout this work is *MURaM* (Vögler et al. 2005, Rempel 2014, 2017), a 3D radiative-MHD code that solves the conservative MHD equations for compressible, partially ionized plasma. It uses a multi-group radiative transfer scheme with short characteristics (Nordlund 1982). The equations for mass (ρ - density), momentum ($\vec{v}$ - velocity, p - pressure), and energy (ϵ_h - enthalpy density) conservation are solved, along with the induction equation ($\vec{B}$ - magnetic field)

$$\partial_t \rho = - \nabla \cdot (\rho \vec{v}), \tag{2.1}$$

$$\partial_t (\rho \vec{v}) = - \nabla \cdot (\rho \vec{v} \vec{v}) - \nabla p + \rho \vec{g} + \vec{F}_{\mathrm{SR}} + \vec{F}_{\mathrm{L}}, \tag{2.2}$$

$$\begin{aligned} \partial_t (\epsilon_h + \rho v^2/2) = &- \nabla \cdot (\vec{v}(\epsilon_h + p + \rho v^2/2)) + \\ & \vec{v} \cdot (\vec{g} + \vec{F}_{\mathrm{L}} + \vec{F}_{\mathrm{SR}}) + Q_{\mathrm{rad}} + Q_{\mathrm{res}} \end{aligned}, \tag{2.3}$$

$$\partial_t \vec{B} = \nabla \times (\vec{v} \times \vec{B}). \tag{2.4}$$

Here, $\vec{F}$ refers to forces and Q refers to source terms. The subscript SR refers to semi-relativistic "Boris correction"-related terms (Boris 1970, Gombosi et al. 2002), which are negligible for our setups, and L refers to the Lorentz force. The two Q terms in the energy equation account for the radiative heating/cooling and resistive heating (since the hydrodynamic energy is conserved, instead of the total energy). For details, we refer the reader to Rempel (2014, 2017). In this work, the grey approximation is used for solving the radiative transfer equations, where the frequency dependence of the opacity is replaced by an average value. This is an acceptable approximation for this work since we are mainly interested in the structure below and just above the surface (Vögler et al. 2004).

Finally, the FreeEOS equation of state (Irwin 2012) with solar abundances (Asplund et al. 2009) is used to close the set of equations.

The effective temperature (T_{eff}) (related to the radiative output), the surface gravitational acceleration (g), related to the hydrostatic balance, and the metallicity (Z) together uniquely specify the spectral class of a star. The *MURaM* code uses a constant gravitational acceleration g, the gas pressure at bottom boundary (p_{bot}), and the inflow entropy at the bottom boundary (s_{bot}) as free parameters. The p_{bot} and s_{bot} parameters determine the height of the $\tau = 1$ surface and the T_{eff}.

2.2.2 Setup and parameters

We considered four stellar cases: F3V, G2V, K0V, and M0V, chosen to cover a broad range of T_{eff} for stellar types with convective envelopes. All boxes have the same number of grid-points (512×512 in the horizontal direction and 500 in the vertical direction). The scaling for the horizontal and the vertical geometric extent was done such that the number of granules in each box is roughly the same and the number of pressure scale heights below the photosphere is also similar (~ 7.5). For the G-star, this corresponds to 4 Mm below the surface and a horizontal extent of 9 Mm $\times$ 9 Mm.

Table 2.1: Parameters for the simulation setup

Type	$z_{\downarrow}*(z_{\text{tot}})$ (Mm)	x_0, y_0 (Mm)	$\Delta x, y$ (km)	Δz (km)	$\log_{10} g$ (cm/s^2)	$(T_{\text{eff}})_{HD}*$ (K)	$(T_{\text{eff}})_{\text{SSD}}*$ (K)	$\langle \|B\| \rangle_{\tau=1}*$ (G)	$\langle |B_z| \rangle_{\tau=1}*$ (G)	$\langle \|B\| \rangle_{\langle\tau\rangle=1}*$ (G)
F3V	11.11 (13.00)	23	45	26	4.301	6817$\pm$7	6807$\pm$8	188$\pm$15	93$\pm$8	132$\pm$10
G2V	4.09 (5.00)	9	17.5	10	4.438	5834$\pm$9	5840$\pm$9	127$\pm$12	66$\pm$6	113$\pm$10
K0V	2.05 (2.31)	4.62	8.2	4.62	4.609	4668$\pm$5	4671$\pm$5	103$\pm$6	50$\pm$3	103$\pm$6
M0V	0.90 (1.14)	2.043	3.99	2.28	4.826	3825$\pm$1	3827$\pm$2	106$\pm$6	54$\pm$4	107$\pm$6

The (*) quantities are determined after running the simulations. The change in T_{eff} will not influence the total radiative output on long timescales ($> 10^5$ yr) corresponding to the Kelvin-Helmholtz timescale. See Spruit (1982) for details.

The boundaries are periodic in the horizontal x, y direction. The top boundary (z_{top}) is open to outflows and closed to inflows, with vertical magnetic fields. The bottom boundary (z_{bot}) is symmetric[1] for mass flux ($\rho\vec{v}$), entropy downflows, and magnetic fields. This magnetic field boundary condition also allows horizontal field to be advected across the bottom boundary. This "mimics" the presence of magnetic field deeper in the convection zone, as considered previously on the basis of equipartition arguments (Rempel 2014, Hotta et al. 2015). The magnetic field BC may not necessarily preserve the $\nabla \cdot \vec{B} = 0$ constraint. However, the hyperbolic divergence cleaning approach (Dedner et al. 2002) employed in *MURaM* takes care of the $\nabla \cdot \vec{B}$ errors reasonably well: $(\nabla \cdot \vec{B})_{\text{rms}}/(\|B\|/\Delta z) \sim O(10^{-3})$; we refer to Fig. A.1 for details.

For each star, we performed simulations with magnetic fields (SSD), and purely hydrodynamic (HD) simulations. HD simulations were initialized with density and internal energy (IE) profiles generated using the 1D stellar code MESA (Paxton et al. 2019) for the F-, K-, and M-star and using the standard solar model from Christensen-Dalsgaard et al. (1996)

---

[1]This refers to the way the derivative is handled across the ghost cells. Symmetric boundary implies the same value in the ghost cell (q_g) next to the boundary domain cell (q_d), such that the derivative across the boundary is zero ($q_g = q_d$), and anti-symmetric implies a value with the opposite sign ($q_g = -q_d$)

for the G-star. These were then run for several hours in stellar time till convection became relaxed and there were no transients visible in velocity and pressure vertical slices. Then the simulation box was seeded with net zero-flux magnetic field with a negligibly small field strength (10^{-5} G) and run till photospheric magnetic field strength reached saturation. The results presented in the subsequent sections are averaged over a few hours of stellar time (after saturation), and over a number of snapshots, for all the eight cases (see Table 2.3 for further details for each setup).

Table 2.1 describes the detailed setup for all the simulations: for all four stellar types, it gives the height of the $\tau = 1$ surface above the bottom boundary (and the total vertical extent), the horizontal extent, the horizontal resolution, the vertical resolution, the log constant surface gravity, the effective temperature of the SSD and HD cases, the average magnetic field magnitude at the $\tau = 1$ iso-surface[2] $\langle\|B\|\rangle_{\tau=1}$, the average unsigned vertical field at the $\tau = 1$ iso-surface $\langle|B_z|\rangle_{\tau=1}$, and the average magnetic field magnitude at the $\langle\tau\rangle = 1$ horizontal slice $\langle\|B\|\rangle_{\langle\tau\rangle=1}$ of the SSD cases. The effective temperature is calculated by averaging the angle-averaged bolometric luminosity over time.

2.3   Results

Star	SSD			HD		
	Color	N	t (h)	Color	N	t (h)
F3V	Blue	264	12.4	Light Blue	124	14.8
G2V	Black	178	7.7	Gray	117	15.0
K0V	Green	125	10.6	Lime	193	16.8
M0V	Red	263	5.4	Light Red	197	10.1

Table 2.2: Color-coding for the plots, along with number of snapshots considered and total time in hours for each stellar box. All HD plots are dashed lines.

All the magnetic simulations exhibit dynamo action and develop magnetic fields with energy within an order of magnitude of the kinetic energy (KE) through most of the simulation box. The change in the partition of energy influences the internal structure as well as convective velocities. Snapshots of the bolometric intensity and vertical velocity at the $\tau = 1$ surface for the SSD and the HD setups (along with the vertical magnetic field for the SSD cases) are shown in Fig. 2.1. The SSD cases show distinct intergranular bright points which correspond with strong magnetic field concentrations. In the following subsections, we examine the horizontally averaged structure of the magnetic field and its effects on the stratification as well as convection for these stellar types. The analysis of the magnetic fields in the lower photosphere and their effect on the bolometric intensity and vertical velocity will be covered in the next paper in this series.

All 1D plots are averages over a number of snapshots spanning a few hours of stellar time (see Table 2.3 for exact numbers). The error bars are standard error (standard deviation normalized by the square root of the number of snapshots $\sigma/\sqrt{N}$) of the average 1D

---

[2]This is the surface corresponding to where $\tau = 1$ in each vertical column of the simulation cube, and this is usually somewhat corrugated because downflows are cooler than upflows and opacity is extremely sensitive to temperature in the relevant ranges.
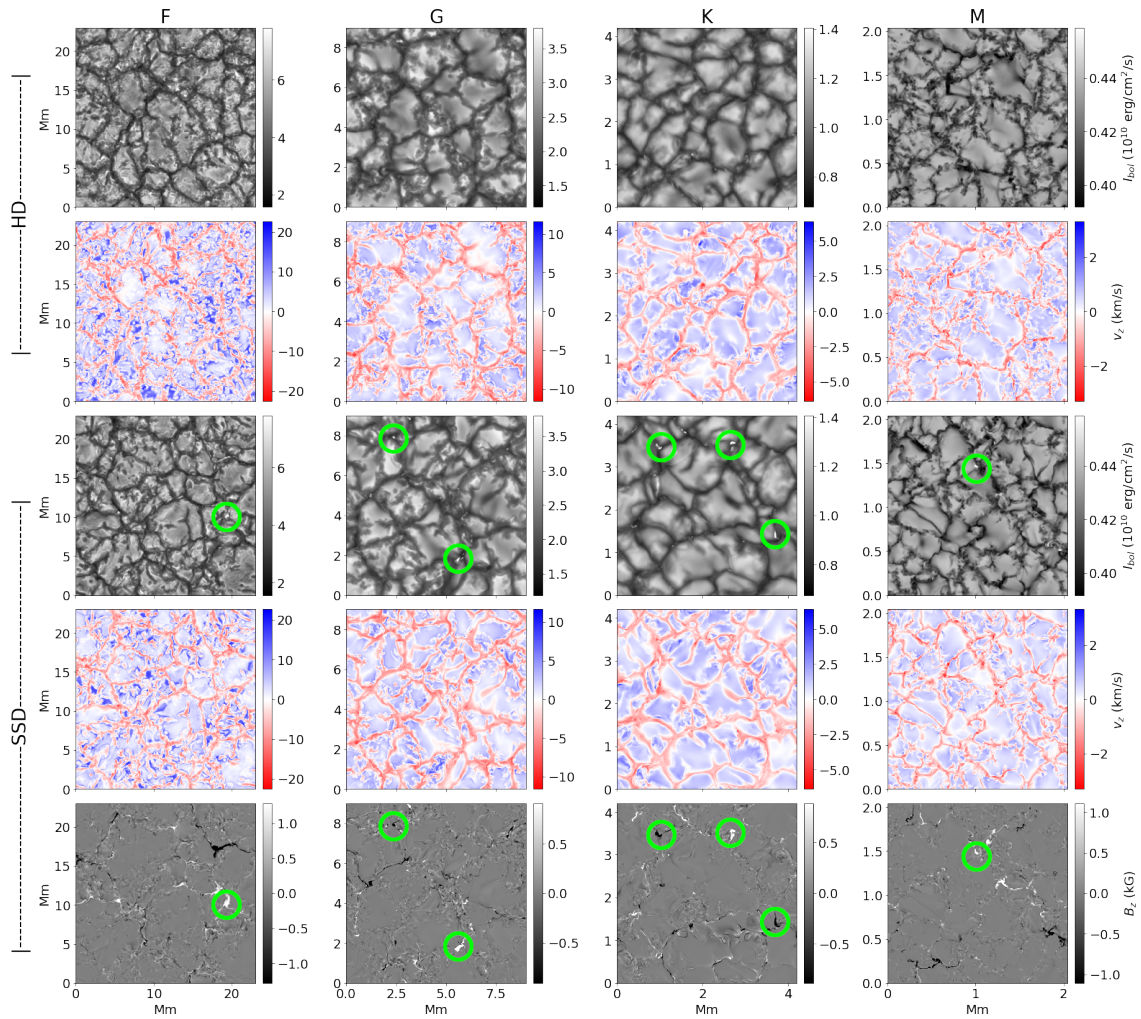
Figure 2.1: Emergent intensity and surface vertical velocities in different stellar types for models with and without magnetic field. *From top to bottom:* Snapshot of the bolometric intensity and v_z at $\tau = 1$ for the HD case (*rows 1 and 2*), bolometric intensity and v_z at $\tau = 1$ for the SSD case (*row 3 and 4*), and the corresponding vertical magnetic field at $\tau = 1$ (*row 5, from left to right*) for spectral types F, G, K, and M, respectively. The green circles indicate the bright points and corresponding magnetic field concentrations.

structure, the assumption being that over this time span, the snapshots are statistically independent.

All quantities are plotted as a function of number of pressure scale heights relative to the height where $\langle\tau\rangle = 1$, $n_H = \log(p_{gas}/p_{gas(\langle\tau\rangle=1)})$. We note that with this definition, positive values correspond to the interior. Since the non-magnetic bottom boundary conditions are identical (p_{bot} and s_{bot} are the same) for HD and SSD runs, the deviations are calculated geometrically and plotted against the corresponding HD pressure scale axis.

This extent in terms of pressure scale heights ranges from 7.5 (bottom) to -5 (near top) for all the simulations. Since the focus of this paper is on the near surface convection zone, we excluded the portion of the box corresponding to $n_H < -1$ from our analysis. We also excluded the region corresponding to $n_H > 6$ due to possible numerical bottom boundary
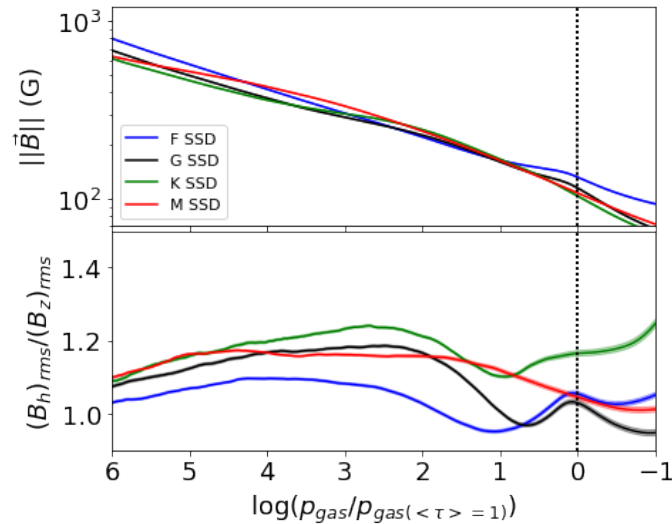
effects.

2.3.1 Magnetic field structure

Figure 2.2: Magnetic field structure for the four stellar cases. *Top:* Horizontally averaged magnetic field magnitude. *Bottom:* The ratio of the horizontal rms field strength to the vertical r.m.s field strength. The horizontal axis is the number of pressure scale heights $\log_{10}(p_{\rm gas}/p_{\rm gas(\tau=1)})$, calculated for the HD cases, below the surface (*dotted vertical black line*). The shaded regions correspond to 1-σ standard error ($e = \sigma/\sqrt{N}$, N is the number of snapshots) computed over time averaging of snapshots.

As mentioned in the introduction to this section, the dynamo action results in a significant amount of magnetic field, with the overall magnitude roughly similar for all the cases, and with a somewhat decreasing trend with $T_{\rm eff}$ near the surface (Fig. 2.2, top panel and last column of Table 2.1). The relation of the magnetic energy (ME) to kinetic energy is discussed in §2.3.3.

The bottom panel of Fig. 2.2 shows the ratio B_h/B_z, which gives an indication of the 3D structure of the magnetic fields. For a fully isotropic distribution of magnetic field, one would expect $B_x^2 \approx B_y^2 \approx B_z^2$. This implies that the ratio of the horizontal r.m.s. component of the magnetic field fluctuations $B_{\rm h,rms}$ to the vertical component $B_{\rm z,rms}$ should be $\sim \sqrt{2}$. For G-, K-, and M-stars, this ratio is slightly less than $\sqrt{2}$ in the middle of the box ($2 < n_H < 5$), indicating near-isotropy, whereas for the F-star, it is significantly lower (~ 1).

Near the $\tau = 1$ surface, $B_{\rm h,rms}/B_{\rm z,rms}$ for all the stars is lower because of intensification of vertical magnetic fields in the intergranular lanes (e.g., Spruit (1979)).

2.3.2 Changes in stratification

Figure 2.3 shows the plots of deviation from the mean HD stratification. The deviations from the HD simulations are presented as the relative percent change in the horizontally
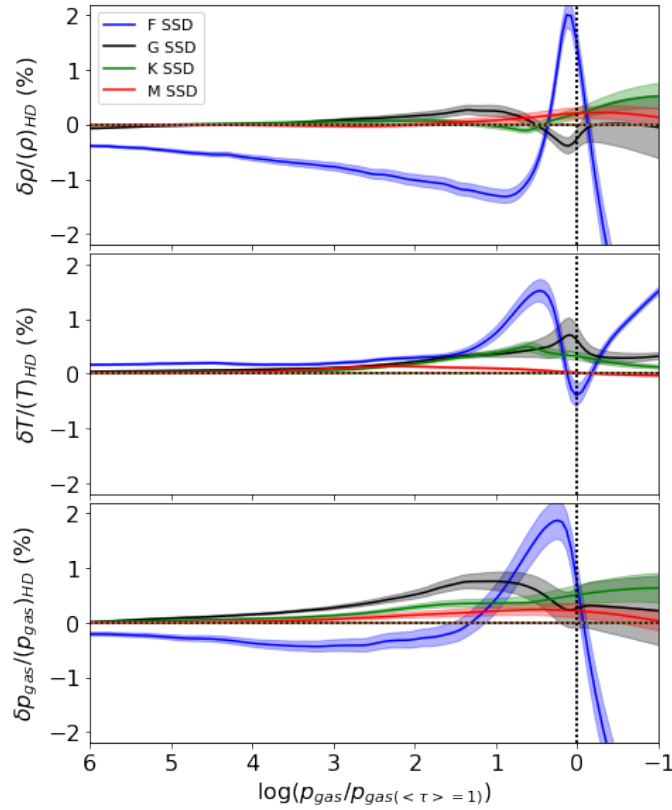
Figure 2.3: Deviations in ρ, T, and p_{gas} for F (*blue*), G (*black*), K (*green*), and M-star (*red*) cases. The vertical axis gives the geometric deviations as a percentage relative to the hydrodynamic case. The horizontal axis is the number of pressure scale heights $\log_{10}(p_{\text{gas}}/p_{\text{gas}(\tau=1)})$, calculated for the HD cases, below the surface (*dotted vertical black line*). The shaded regions correspond to 1-σ standard error ($e = \sigma/\sqrt{N}$, N is the number of snapshots) of the mean solid curve.

averaged 1D structure. For any quantity of interest q (e.g., density, temperature, etc.), these deviations are calculated as $(q_{\text{SSD}} - q_{\text{HD}})/q_{\text{HD}}$. This means that a positive value for the deviation corresponds to a higher value for the SSD case relative to the HD case.

All simulations show slight ($\leq 2\%$) changes in thermodynamic stratification relative to the corresponding HD simulations, with the magnitude of deviations below the surface roughly increasing from coolest to hottest stellar type. Below 3 pressure scale heights, the G, K, and M simulations show negligible ($\leq 0.1\%$) deviations in thermodynamic quantities.

Closer to the surface, the F-star simulation shows up to 1.5% reduction in density and up to 1% reduction in gas pressure (Fig. 2.3, top and bottom panels, blue line). This trend is opposite to that seen for other cases, all of which show a slight ($< 1\%$) enhancement in density and pressure. These results are analyzed in §2.4.1. For context, a 1.5% deviation in temperature for an F-star would correspond to a temperature change of $\sim$100 K.
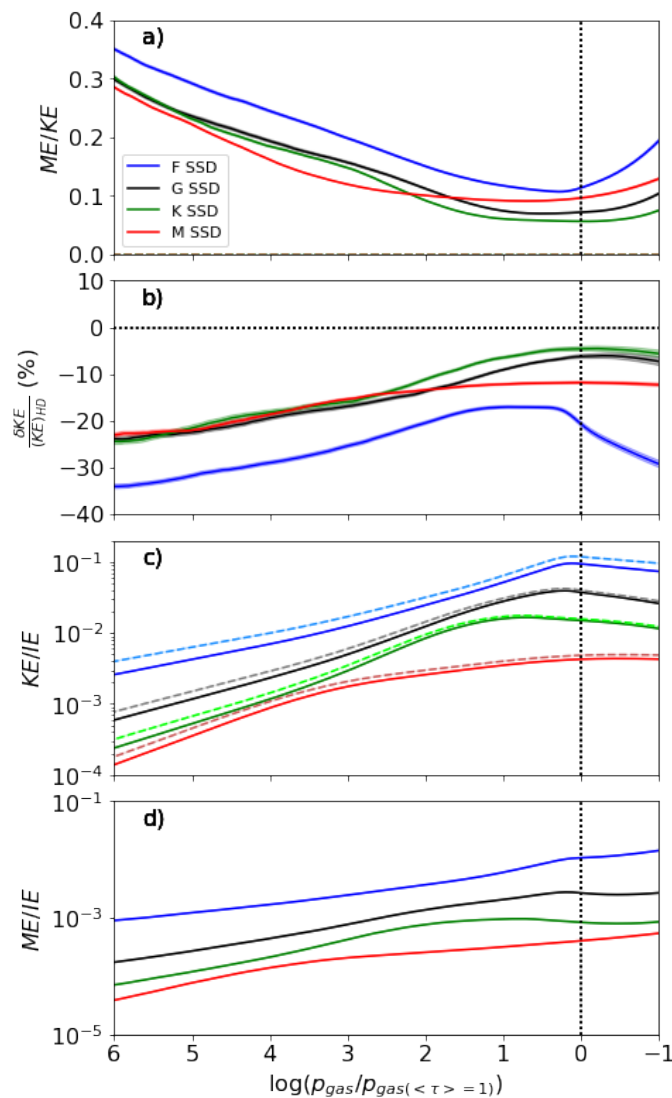
Figure 2.4: Distribution of energies for the four stellar cases. a) Ratio of ME to KE, b) percent change in KE, c) ratio of KE to IE, and d) ratio of ME to IE (*bottom*) for F-, G-, K-, and M-stars.

2.3.3 Distribution of energies

In Fig. 2.4, panel a shows the ratio of magnetic to kinetic energy. For all cases, this ratio is within an order of magnitude throughout the box. This ratio for the F-star is significantly higher compared to the other stars. In addition, the ratio for M-star has a minima deeper down in the box than for other stars. As before, the general trend shows a decrease in this ratio with decreasing T_{eff}.

In Fig. 2.4b, we shows the relative change in KE between the SSD and the HD setups. All stars show a marked decrease in KE in the SSD case. As with the top panel, F-star shows a significantly stronger reduction in KE compared to the other cases. The M-star as well shows a stronger reduction in KE near the surface compared to the G and K-stars.

Fig. 2.4c shows the ratio of kinetic to internal energy. For the F-star, this ratio is within

an order of magnitude near the surface, whereas for the other stars, it is less than 1%. Fig. 2.4d shows the ratio of the magnetic to the internal energy. There is a clear trend in this ratio with stellar type, with it being lowest for M-star ($\sim 5 \times 10^{-5}$ near bottom, to $\sim 10^{-4}$ near surface) and highest for F-star ($\sim 10^{-3}$ near bottom, to $\sim 10^{-2}$ near surface).

2.3.4   Changes in velocities
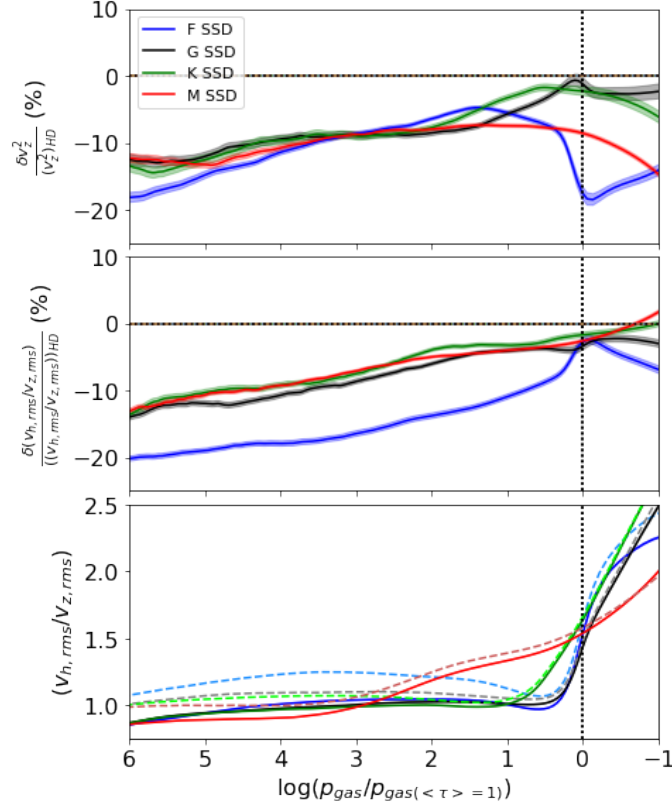
Figure 2.5: Relative decrease in convective velocities v_z^2 (*top*), relative decrease in ratio of horizontal to vertical rms velocities $v_{h,rms}/v_{z,rms}$ (*middle*) and the actual $v_{h,rms}/v_{z,rms}$ ratio (*bottom*).

All SSD cases exhibit a decrease in vertical velocities v_z^2 as well as the ratio of horizontal to vertical rms velocities $v_{h,rms}/v_{z,rms}$ (Fig. 2.5), relative to the corresponding HD cases. The reduction in v_z^2 follows similar trend for all the four stars, with a decrease of 4-8% near the surface, going up to 20% near the bottom boundary. For G-, K- and M-star, the decrease in $v_{h,rms}/v_{z,rms}$ is similar (5% near the surface, going up to 12% near the bottom) but is more pronounced for the F-star case (10% near the surface, going up to 20% near the bottom boundary). This implies a change in the horizontal extent of sub-surface granulation, which follows Nordlund et al. (2009), who showed using simple mass conservation that the horizontal extent of granules is proportional to $H(v_h/v_z)$, where H is the local density scale height.

The ratio $v_{h,rms}/v_{z,rms}$ gives an idea of the 3D velocity structure. Close to the $\tau = 1$ surface, the ratio increases suddenly. This increase corresponds to where convective flows turn

over, as the atmosphere becomes convectively stable and the flows above that point are mainly due to convective overshoot. The exact pressure scale depth where this turning over takes place depends of the effective temperature: for the F- and G-star, this turnover takes place within half a pressure scale height of the $\tau = 1$ surface whereas, for the M-star, it takes place well below the $\tau = 1$ surface (around $n_H = 3$). This is also probably why the minima of the ME/KE ratio in Fig. 2.4 for M-star is significantly below the surface compared to the G and K-star, as density (and, consequently, KE) is lower above the height where most of the overturning takes place. The changes in v_z^2 as well as the $v_{h,rms}/v_{z,rms}$ with depth seem to follow a regular trend, and is consistent with the results obtained previously in whole-convection zone simulations with a small-scale dynamo setup (Hotta et al. 2015).

2.4 Discussion

2.4.1 Turbulent pressure
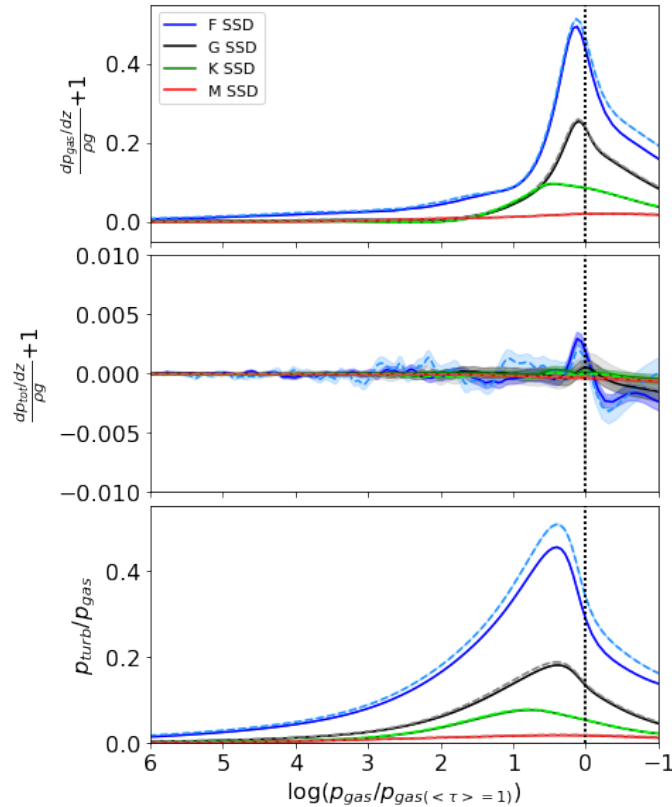
Figure 2.6: Hydrostatic force balance with gas pressure p_{gas} (*top*) and total pressure p_{tot} (*middle*) gradient term and ρg term, normalized by $\langle \rho g \rangle$ as $\langle dp/dz + \rho g \rangle / \langle \rho g \rangle$, and the ratio of turbulent pressure to gas pressure (*bottom*). All quantities are plotted for SSD (*solid*) and HD (*dashed*) cases. We note that the extent of y-axis is larger by more than an order of magnitude for force balance with p_{gas} compared to force balance with p_{tot}

We first discuss the changes in the pressure and density in the SSD models relative to a

purely HD model. The pressure and density changes (Fig. 2.3) are very small ($\sim 0.1\%$) for the G-, K-, and M-star in the convection zone (and not significantly greater near the surface for the K- and M-star). The changes are more prominent for the F-star ($\sim 1\%$). This discrepancy can be understood by considering the contribution of turbulent pressure in the overall hydrostatic balance.

Turbulent pressure becomes important for hydrostatic balance when KE is within an order of magnitude or so of the IE. This is indeed the case for our F-star models. This implies that turbulent pressure (which is largely due to plasma motions) can be a significant fraction of the gas pressure p_{gas}. Quantitatively, this can be seen from a crude MLT calculation of the Mach number (see appendix A.1 for derivation):

$$M \approx 0.138 \left(\frac{T}{10^3 \text{ K}}\right)^{5/6} \left(\frac{\rho}{10^{-7} \text{ g/cm}^3}\right)^{-1/3}. \tag{2.5}$$

Using the above equation, we calculate the F-star photospheric Mach number to be about 0.75 (see Table 2.4.1), slightly lower than simulation value in Beeck et al. (2013a) who found it to be 0.9. For the other stars, the velocity is decidedly subsonic.

Simulation	T_{surf} (10^3 K)	ρ_{surf} (10^{-7} g/cm^3)	M
F3V	6.19	0.59	0.75
G2V	6.17	2.39	0.47
K0V	4.94	6.67	0.28
M0V	3.96	21.3	0.16

Table 2.3: Mach numbers computed using MLT. ρ_{surf} and T_{surf} are obtained from HD simulation data.

Now, the hydrostatic balance is expressed in terms of the balance between force due to pressure gradient, $p' = dp/dz$, and gravity, ρg, acting in the vertical (viz. radial) direction. These two terms should be approximately equal in magnitude. If just p_{gas} is considered, this balance does not hold very well, with deviations increasing strongly with T_{eff} (Fig. 2.6, top panel).

The turbulent pressure consists of terms from the total stress tensor. From Reynolds stresses, the $\rho v_i v_j$ term and from Maxwell stresses, the $((B^2/2)\delta_{ij} - B_i B_j)/4\pi$ term is obtained. As mentioned in the introduction, the presence of SSD magnetic fields implies a reduction in KE, where energy is redistributed between the plasma motions and magnetic fields via Lorentz force feedback. In Fig. 2.4, the ratio of ME to KE (top panel) corresponds remarkably well with the reduction in KE relative to the HD case (middle panel), implying most of the energy in the magnetic fields is drawn from the KE reservoir. The ME is within an order of magnitude of the KE for subsurface plasma. This is consistent with the results on equipartition of energy in several SSD simulations (Hotta et al. 2015, Haugen et al. 2004, Schekochihin et al. 2004b).

This order of magnitude equipartition results in a reduction of plasma velocities and, consequently, the magnitude of the Reynolds stress term. The contribution from the Maxwell stress, on the other hand, can be either negative or positive, depending on whether the effects of magnetic tension dominate over that of magnetic pressure in the vertical direction. More quantitatively (see Appendix A.2 for a derivation), the total turbulent pressure can be expressed as:

$$p_{\text{turb}} = \rho v_z^2 + \frac{B_h^2 - B_z^2}{8\pi}. \tag{2.6}$$

With this included in the calculation of the pressure gradient term, the hydrostatic balance is satisfied, as can be seen in middle panel of Fig. 2.6 (noting the difference in the extent of y-axis for the top and middle panels). In the bottom panel of the same figure, the reduction in $p_{\text{turb}}/p_{\text{gas}}$ is most prominent for the F-star. Since the changes in v_z^2 are similar (Fig. 2.5, top panel) for all stars, there must be a reduction in density for the F-star to compensate for the significant change in p_{turb}. Based on the expression for p_{turb}, we introduce an effective turbulent velocity $v = \sqrt{p_{\text{turb}}/\rho}$.

With this, it becomes possible to relate changes in density stratification to changes in total pressure gradient. A straightforward consideration of the density scale height H_ρ (see appendix A.2) yields:

$$H_\rho = RT/(\mu g) + v^2/g. \tag{2.7}$$

This tells us that where $B_h^2 < B_z^2$ and $(\rho v_z^2)_{\text{SSD}} < (\rho v_z^2)_{\text{HD}}$, the scale height of the SSD model is smaller than for the HD model, $(H_\rho)_{\text{SSD}} < (H_\rho)_{\text{HD}}$. This is valid if assuming that the change in T and μ is relatively small. From the proportionality between density scale height and v_z^2 (Eq. 2.7), the decrease in vertical velocity is associated with a decrease in the local density scale height. This can be inferred from Fig. 2.6 (bottom panel), where the ratio $p_{\text{turb}}/p_{\text{gas}}$ ($\propto v^2/(RT/\mu)$) is noticeably lower for F-star near the surface.

These conditions are satisfied relatively well for the F-star case. A decrease in H_ρ implies a steepening of the density stratification for the SSD case relative to the HD case. This is exactly the case in the top panel of Fig. 2.3: the reduction in density goes from a $\sim 0\%$ to $\sim 1.5\%$ near the surface. Below the surface, it is reasonably good to assume a perfect gas equation of state, with $p_{\text{gas}} \propto \rho T$. Assuming changes in T are small compared to ρ and p_{gas}, this, in turn, implies that the changes in p_{gas} follows a similar trend as changes in ρ. Near the surface, this picture breaks down since the mode of energy transfer changes from convective to radiative and this simplified analysis is no longer valid.

The effect of turbulent pressure on stratification and convection has previously been considered for stellar model envelopes from an MLT perspective (Henyey et al. 1965) as well as for 3D HD simulations (Ludwig and Kučinskas 2012, Jørgensen and Weiss 2019); however, to the best of our knowledge, the effect of magnetic fields from an SSD have not been considered before.

2.4.2   Changes in velocity structure

As mentioned in §2.3.4, the ratio $v_{\text{h,rms}}/v_{\text{z,rms}}$ (Fig. 2.5, bottom panel), gives an idea of where convection overturns relative to pressure scale height for a given effective temperature. The trend in overturning for different spectral types fits the usual picture of "hidden" granulation below the $\tau = 1$ surface for cooler, denser stars such as M and K versus the "naked" granulation above the $\tau = 1$ surface of hotter, more rarefied stars such as G and F, as discussed in Nordlund and Dravins (1990).

This ratio is close to 1 for the HD G-, K-, and M-stars (dashed lines). For the HD F-star, however, it is significantly higher (dashed light blue line), indicating a higher degree of

isotropy in the velocity structure[3]. This implies relatively higher horizontal velocities for the HD F-star. The near-isotropic velocity profile for the HD F-star can be attributed to the KE being a non-negligible fraction of the IE. We speculate that these stronger horizontal velocities contribute to the stronger magnetic fields in the vertical direction for the F-star (as inferred from the lower $B_{h,rms}/B_{z,rms}$ for the F-star in Fig. 2.2, bottom panel).

In the case of SSD (solid lines), all stars follow a similar trend for $v_{h,rms}/v_{z,rms}$, with the ratio being ≤ 1 up to the point where convection overturns. The change in velocity field structure in the presence of SSD fields is a hard problem that depends on the SSD saturation mechanism. We note that the $B_{h,rms}/B_{z,rms}$ ratio is lower for F-star compared to other cases. It is plausible that the relatively stronger fields in the vertical direction restrict horizontal flows more in the case of F-stars and lead to a greater change in the value of $v_{h,rms}/v_{z,rms}$. However, a fuller understanding of this behavior requires a more detailed analysis that is beyond the scope of this paper.

2.5 Conclusions

In this work, we investigate the magnetic field self-consistently generated by an SSD acting in the near-surface layers of main-sequence stars of spectral types F3V, G2V, K0V, and M0V. The SSD mechanism operates in all cases to amplify magnetic fields from a seed field of negligible strength and zero net flux. The magnetic fields from the SSD have an energy density that is a non-negligible fraction of the kinetic energy density. These fields act back on the plasma to reduce the convective velocities, which in turn reduces the turbulent pressure. This becomes substantial for the F-star as it is hot enough to have kinetic and internal energy within an order of magnitude near the surface, which gives magnetic fields stronger than those in G-, K-, and M-stars, especially in the vertical direction. The equation for hydrostatic balance for total pressure and the reduction of convective velocities implies a reduction in the density scale height itself. This is significant enough for the F-star to result in reduced density and gas pressure throughout the box. This effect tends to get smaller towards later spectral types.

This paper only covers the near-surface convection zone. Other aspects of particular interest to observational studies would include the magnetic field structure in the lower photosphere and changes in the intensity characteristics. In addition, the change in scale height and the changes in v_h/v_z imply changes in granulation scale. All these points are to be investigated in a follow-up paper.

---

[3]Fully isotropic flow requires $v_x^2 = v_y^2 = v_z^2$. Hence, this would imply $v_{h,rms}/v_{z,rms} = \sqrt{2}$

3 Changes in the photospheres of main-sequence stars

The contents of this section correspond to a draft article to be submitted to A&A by Bhatia, T. S., Cameron, R. H., Peter, H., et al. I ran the simulations, performed the analysis and wrote the majority of the text.

Abstract

Context: Some of the quiet solar magnetic flux could be attributed to a small-scale dynamo (SSD) operating in the convection zone. For an SSD operating in cool main-sequence stars, the associated magnetism could affect the granulation signal as well spectral line shifts.

Aim: We aim to investigate the distribution of SSD magnetic fields as well as their effect on bolometric intensity characteristics, vertical velocity and spatial distribution of kinetic energy (KE) and magnetic energy (ME) in the lower photosphere of different stellar types.

Methods: We analyze the four simulation sets for F-,G-,K- and M-stars described in Bhatia et al. (2022) near the $\tau = 1$ layer. We compare the time-averaged distributions and power spectra in SSD setups relative to the hydrodynamic setup.

Results: The SSD field strengths for all cases follow a roughly similar distribution, with average fields around 100 G for the G-,K- and M-star, and somewhat higher for the F-star. These fields also result in magnetic bright points and a decrease in upflow velocities for all stellar types. Lastly, the changes in spatial KE spectrum is similar for all cases as well, with a decrease in energy at subgranular scales as well as the largest scales.

Conclusion: The effects of SSD fields on all spectral types, when compared to a pure hydrodynamic model, are rather similar. The strength and distribution of magnetic fields are roughly similar for the different stellar types, which is a consequence of similar photospheric KE for all cases and a rough equipartition between KE and ME. All stellar types exhibit magnetic bright points and a slight reduction in granule sizes for the SSD models. There is a decrease in a proxy convective blueshift based on bolometric intensity, with the magnitude of change scaling with T_{eff} for the SSD runs compared to the non-magnetic models.

3.1   Introduction

Magnetism in cool stars is ubiquitous. In addition, a significant number of cool stars show a solar-like activity cycle (Wilson 1978). The magnetic fields associated with these cycles are expected to arise from a large-scale dynamo operating in the convection zones of cool stars (Brandenburg and Subramanian 2005b, Charbonneau 2014). However, there is also an additional, cycle-independent component of stellar fields, the quiet-star magnetism. From detailed observations of the quiet Sun (Solanki 1993, de Wijn et al. 2009, Sánchez Almeida and Martínez González 2011, Bellot Rubio and Orozco Suárez 2019) as well as state-of-the-art simulations (Vögler and Schüssler 2007, Rempel 2014), this component was realized to be substantial and could, in part, be explained by invoking a small-scale dynamo (SSD) mechanism which would amplify magnetic fields via turbulent motions of the plasma. In fact, recent global SSD simulations (Hotta and Kusano 2021) showed that the field generated can be significantly super-equipartition in the deep convection zone, being strong enough to affect the meridional circulation and the differential rotation profile. For solar-like stars, the influence of SSD fields on quiet star phenomenon like the granulation signal remain yet to be studied.

Stellar photometry observation missions have increasingly expanded in scope and sensitivity. NASA's CoRoT and *Kepler*/K2 exoplanet-hunting missions heralded a new era in exoplanetary science, enabling detection of thousands of exoplanets through precise and long-term observations. Currently, NASA's TESS (Ricker et al. 2014) and ESA's PLATO (Rauer et al. 2014) missions are expected to drastically increase the detection rate of rocky planets around bright M- and FGK-dwarfs, respectively. In the era of high-precision and high-cadence photometry, it is essential to understand the factors that affect stellar brightness variations and radial velocity (RV) measurements from spectrographs like HARPS (Pepe et al. 2004) and, now, ESPRESSO (Pepe et al. 2021).

RV measurements allow detection of exoplanets by accounting for Doppler shifts in stellar spectral lines due to a gravitationally-induced "wobble" caused by the planet's orbital motion. However RVs can be affected by stellar magnetism (e.g., starspots, faculae) and well as the granulation signal, which is visible as a net blueshift in lower photospheric spectral lines of most solar-like stars (Dravins 1987). For a comprehensive list of factors potentially affecting high precision RV measurements, see Table A-4 in Crass et al. (2021). Shporer and Brown (2011) demonstrated the impact convective blueshift can have on RV measurements during transits at m/s accuracy level via a simple model. With RV measurements reaching sub-m/s precision, potentially allowing detection of Earth-like rocky exoplanets, it becomes imperative to understand the sources of stellar "noise" properly, including the contribution from magnetic fields. For the solar case, Shapiro et al. (2017) showed that total solar irradiance (TSI) could be reliably reconstructed just from the consideration of granulation noise from simulations and solar magnetograms in a forward model. This is encouraging for modelling stellar variability at shorter timescales.

In addition, the granulation flicker, that is, the amplitude of stellar brightness over timescales of granulation (< 8 hours), shows an observational correlation with surface gravity (Bastien et al. 2013). This allows an independent method (apart from astroseismic measurement) of determining surface gravity for a large sample of stars. However, there are some inconsistencies between models and observations for stars with $T_{\text{eff}} > 6650$ K (Bastien et al. 2016). This could be resolved by better models of stellar convection and granulation.

In our recent work (Bhatia et al. (2022), hereafter Paper I), we showed that SSD magnetic fields significantly reduce the convective velocities and can be strong enough in hotter spectral types (F-star and above) to even affect the stratification and scale heights near the surface. Hence it becomes imperative to understand the effect of SSD fields on the photosphere.

In this paper, we describe the distribution of photospheric quiet-star magnetic fields as expected to arise from an SSD mechanism. We also look at the effects of this magnetic field on the bolometric intensity as well as energy distribution in the photosphere.

3.2   Methods

We use models described in Paper I, namely, the hydrodynamic (HD) models and the models with the small-scale dynamo (SSD) fields. The setup, number of snapshots, time range etc. are identical as in Paper 1.

Before we start describing the results, there is a quick note regarding the meaning of symbols and conventions we follow. All averages over time are denoted by an overline $\overline{q}$. All averages over space of 2D data are denoted by angular brackets $\langle q \rangle$. The standard deviation for bolometric intensity in a single snapshot is calculated as $\sigma_I = \sqrt{\langle (I - \langle I \rangle)^2 \rangle}$. The calculation of spatial power spectra is covered in Appendix B.1. All plots have error bars corresponding to standard error $\epsilon = \sigma / \sqrt{N}$, where N is the number of snapshots and σ is the standard deviation over time averages. The color coding is the same as that in Paper I, with blue for F, black for G, green for K and red for M-star. Dashed lines with lighter corresponding colors refer to the hydrodynamic case, unless stated otherwise.

3.3   Results

3.3.1   Distribution of the magnetic fields

Table 3.1: Characteristic of magnetic field near the surface. All values are averages over time along with 1σ standard deviation.

Simulation	$\overline{B}$ [G]		$\overline{\lvert B_z \rvert}$ [G]		$\overline{B_h}$ [G]		$\overline{A_{B>1\mathrm{kG}}/A_{\mathrm{tot}}}$ [%]	
	$z_{\langle \tau \rangle = 1}$	$\tau = 1$	$z_{\langle \tau \rangle = 1}$	$\tau = 1$	$z_{\langle \tau \rangle = 1}$	$\tau = 1$	$z_{\langle \tau \rangle = 1}$	$\tau = 1$
F3V	131 ± 11	188 ± 15	66 ± 7	93 ± 8	99 ± 8	144 ± 11	0.06 ± 0.06	0.79 ± 0.31
G2V	114 ± 11	127 ± 12	59 ± 6	66 ± 6	85 ± 8	96 ± 9	0.46 ± 0.14	0.47 ± 0.14
K0V	102 ± 6	103 ± 6	50 ± 3	50 ± 3	80 ± 5	81 ± 5	0.28 ± 0.08	0.26 ± 0.08
M0V	106 ± 6	106 ± 6	54 ± 4	54 ± 4	81 ± 5	81 ± 5	0.43 ± 0.17	0.41 ± 0.16

Fig. 3.1 shows the horizontally-averaged magnitude (top panel) and horizontally-averaged inclination (bottom panel) of the magnetic field near the surface. All cases show similar value of magnetic field strength, except for the F-star, which shows a somewhat higher value at and above the surface (as marked by the dotted vertical line). The field inclination shows the field becoming more horizontal for all cases as one goes higher up in the atmosphere. Because the top boundary condition forces the field to be purely vertical, and
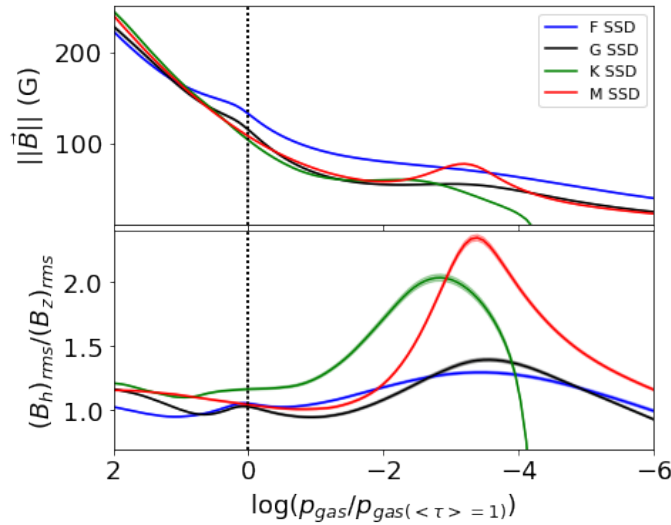
Figure 3.1: Magnetic field characteristics for the SSD F- (*blue*), G- (*black*), K- (*green*) and M-star (*red*). *Top*: Horizontally averaged magnitude of magnetic field . *Bottom*: Horizontally averaged inclination of magnetic field, defined as $\langle \sqrt{(B_x^2 + B_y^2)/B_z^2} \rangle$. The horizontal axis is the number of pressure scale heights below the surface (positive is below, negative is above).

the number of pressure scale heights above the surface are not exactly same for all cases, we do not extend our analysis beyond $\log(p_{\text{gas}}/p_{\text{gas}(\langle\tau\rangle=1)}) > -1$.

Table 3.1 shows the average field strength, average vertical field strength, average horizontal field strength and the fraction of area occupied by kilogauss (kG) fields, for all cases for $\langle\tau\rangle = 1$ horizontal slice as well as for $\tau = 1$ iso-surface[1]. Here, τ refers to the Rosseland mean optical depth, since the radiative transfer is gray. The $\tau = 1$ iso-surface makes sense from an observational point of view. We also consider the horizontal slice because the thermodynamic stratification is expected to be quite uniform in the horizontal direction, allowing a better understanding of the physics of magnetic field distribution. The columns show that for the horizontal slice, the average field strength is quite similar (100 to 130 G) for all cases, but the value increases significantly for the F-star (almost 190 G) and G-star (almost 130 G) if the $\tau = 1$ iso-surface is considered. For the K-, and M-star, there is no change.

Fig. 3.2 shows the probability density function (PDF) of the magnitude of the magnetic field for the horizontal slice at $\langle\tau\rangle = 1$ (top panel) and for the $\tau = 1$ iso-surface (bottom panel). All stars show a rather similar distribution of photospheric magnetic fields $\|\vec{B}\|$, with most of the field around 100 G (slightly higher for the F-star) and a more rapid drop-off in the kG regime.

For the horizontal slice, the sharp drop-off in the PDF in the kG regime shows an inverse trend between T_{eff} and strength of kG fields. These kG field form mostly in the downflow lanes (see Fig. B.2 and B.3 for PDFs of B in upflows and downflows, respectively). There is a rough correspondence between the pressure equipartition field strength $B_{\text{eqp}} =$

---

[1]The $\tau = 1$ iso-surface refers to the surface where $\tau = 1$ for each vertical column in the 3D cube. The data points are calculated by interpolating against the corresponding τ column to where $\tau = 1$.
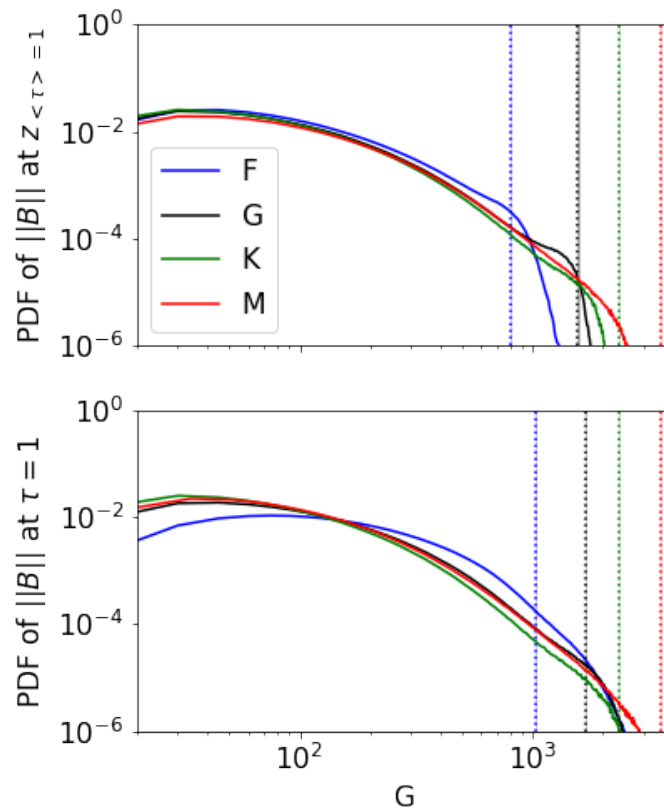
Figure 3.2: PDF of the magnitude of magnetic field $\|B\|$ for the SSD F- (*blue*), G- (*black*), K- (*green*) and M-star (*red*). *Top*: PDF of $\|B\|$ calculated for the geometric surface $z_{\langle\tau\rangle=1}$ corresponding to the height at which $\langle\tau\rangle = 1$. *Bottom*: Same plot as the top, but for the iso-$\tau = 1$ surface. The vertical dotted lines correspond to the pressure equipartition field $B_{eqp} = \sqrt{8\pi p_{gas}}$ for each case.

$\sqrt{8\pi p_{gas}}$ (shown by dotted vertical lines for all stars), and the drop-off, but it does not sufficiently explain the trend. For the F-star, the strongest fields are super-equipartition whereas for the M-star, these are decidedly sub-equipartition.

However, if one considers the $\tau = 1$ iso-surface (bottom panel), the distribution of fields is roughly similar and does not show the trend from the $\langle\tau\rangle = 1$ slice. In addition, the field strengths for the F-star are generally higher. The former can be understood as follows: as the downflows are cooler relative to upflows and the opacity near the surface varies strongly with temperature, the $\tau = 1$ iso-surface forms geometrically deeper in downflows relative to the upflows. Hence, the magnetic field "seen" at this level is deeper than at the $\langle\tau\rangle = 1$ geometric slice. This effect is similar to the Wilson depression (WD) of the optical surface in sunspots. Because of increasing density and pressure due to stratification and conservation of flux, the field strength is stronger deeper down. The magnitude of this depression scales with T_{eff} as well as pressure scale height (Beeck et al. 2015b), and is the strongest for F-star and weakest for M-star.

The factors influencing the kG field distribution are discussed later in the context of convective collapse (Spruit 1979) in Sect. 3.4.1.
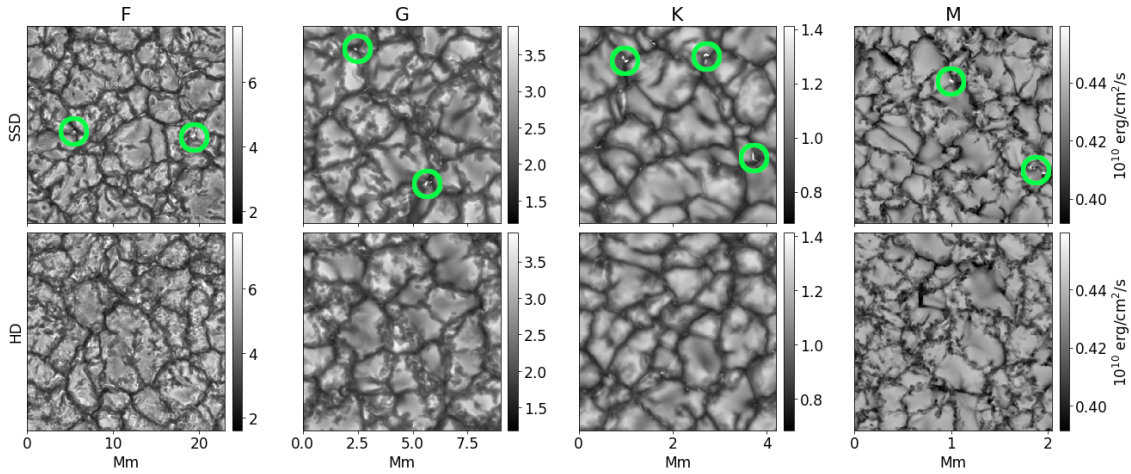
3.3.2 Bolometric intensity

Figure 3.3: Snapshot of the bolometric intensity (in 10^{10} erg/cm^2/s) for the SSD case (*top*), and the HD case (*bottom*) for spectral types (*from left to right*) F, G, K and M, respectively. The colorbars are identical for the respective SSD and the HD case. Green circles indicate magnetic bright points.

Table 3.2: Average values for various quantities related to v_z and I_{bol}. For each quantity, left column is SSD, right is HD. All units are cgs.

Simulation	upflow frac. (%)		$\overline{v_{z,rms}}$ (10^5)		$\langle I_{bol} \rangle$ (10^{10})		$\overline{\sigma_I}$ (10^{10})		contrast (%)	
F3V	57.33	57.14	5.168	5.565	4.710	4.718	1.004	1.027	21.31	21.76
G2V	56.63	56.82	2.518	2.561	2.563	2.556	0.440	0.444	17.17	17.36
K0V	56.09	55.90	1.306	1.326	1.045	1.042	0.122	0.122	11.66	11.71
M0V	60.32	60.04	0.632	0.660	0.425	0.425	0.011	0.011	2.67	2.66

In Paper 1, we considered the changes in thermodynamic structure due to SSD-generated magnetic fields. We showed that these changes resulted in a decrease in density scale height H_ρ, as well as convective velocities, near the surface. Here, we consider how these changes affect the intensity structure.

The presence of SSD magnetic fields affects the bolometric intensity I_{bol} in multiple ways. The evacuation of plasma due to concentrated magnetic fields in intergranular lanes leads to formation of bright points. This is due to heating of the downflow lane plasma from the surrounding hot upflows, also called the "hot-wall" effect (Spruit 1976), where the low density, relatively cold intergranular plasma is heated up by the surrounding hot, dense upflows which causes them to appear bright. This is apparent for F, G, K and (to a lesser degree) M stars (see Fig. 3.3).

In addition, there are changes in the spatial distribution of I_{bol}. The top panel of Fig. 3.4 shows the magnitude of the spatial power spectra P_k (see appendix B.1 for details on how the power spectrum is calculated) of I_{bol} for all the HD and SSD cases. Note that the spatial frequency has been scaled by the box size, which essentially corresponds to a pressure scale height scaling (see Sect. 2.2 of Paper 1 for details). This ensures all plots
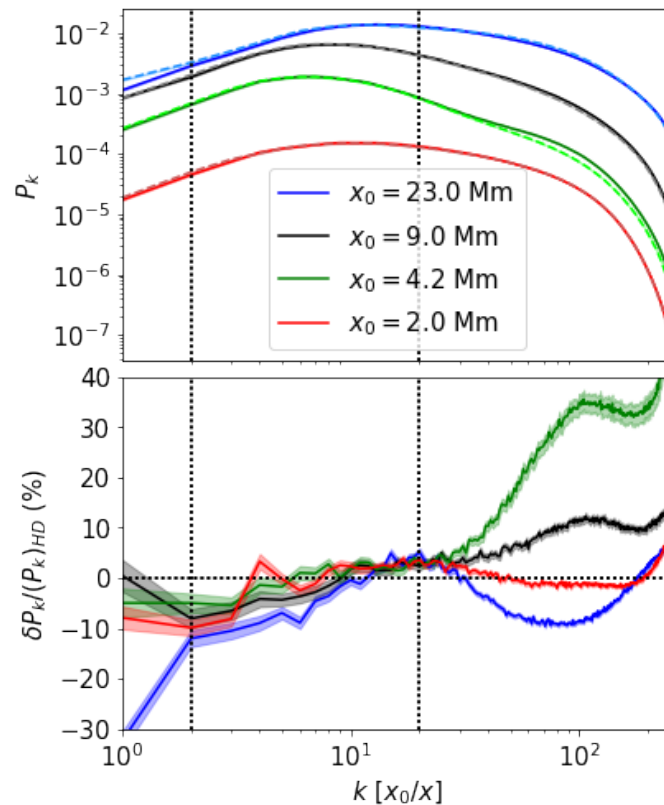
Figure 3.4: Spatial power spectra P_k of bolometric intensity I_{bol} for the SSD (*solid*) and HD SSD (*dashed*) cases plotted against spatial frequency $1/x$ (normalized by the horizontal box size x_0 for each star). *Top*: P_k for all cases normalized by the SSD F-star total power ($\sum_k P_k$). *Bottom*: Relative change in power at different scales between the SSD and HD cases. The vertical dotted lines refer to the approximate scales corresponding to range in granule sizes, for which the center of gravity is calculated in Table 3.3.

have the same range on the *x*-axis (see appendix B.1 for this plot without such scaling). The bottom panel shows the relative change in the power between SSD and HD cases $(P_{k,\text{SSD}}/P_{k,\text{HD}}) - 1$, with positive values corresponding to an increase in power. The usual interpretation of P_k, as calculated here, is in terms of level of contrast at different spatial scales (Nordlund et al. 1997). We take the peaks of these spectra to be an indication of the granulation scales, as the most prominent contrast exists between the granule centers and the intergranular lanes. Due to variation of granule sizes over a range of scales, we calculate the center of gravity (CG) over a range of k (marked by dotted vertical lines) to estimate an average spatial wave number k_{CG} corresponding to an average granule size. The relevant spatial range is between $x_0/x \in (2, 20)$. For reference, this corresponds to a spatial frequency between 0.22 Mm^{-1} and 2.2 Mm^{-1} for the G-star (where the typical granule size is ~ 2 Mm, corresponding to a spatial frequency of 0.5 Mm^{-1}). The results are presented in Table 3.3. We interpret the positive change in k_{CG} for all cases as an indication for a decrease in average granule size for SSD cases, relative to the HD cases.

The effect of SSD fields on intensity at sub-granular scales is more varied between spectral types. Fig. 3.4, bottom panel, shows a prominent increase in power for the K-star at

Table 3.3: Center-of-gravity (CG) for average granulation scale in Fig. 3.4

Simulation	$k_{\mathrm{CG,SSD}}[x_0/x]$	$k_{\mathrm{CG,HD}}[x_0/x]$	$\delta k/k_{\mathrm{HD}}$ (%)
F3V	11.78	11.57	+1.76
G2V	10.76	10.63	+1.25
K0V	9.98	9.90	+1.8
M0V	11.21	11.12	+1.82

the smallest spatial scales, corresponding to the high-contrast bright points present in the intergranular lanes. A similar interpretation also holds for the G-star. Visually, we also see bright points in the F-star case (See Fig. 1 of Paper I for prominent examples). However, these bright points do not lead to an increase in power. This is because magnetic fields also restrict convective velocities, acting as an effective "viscosity", which makes the flow more laminar and leads to granules with a smoother appearance.
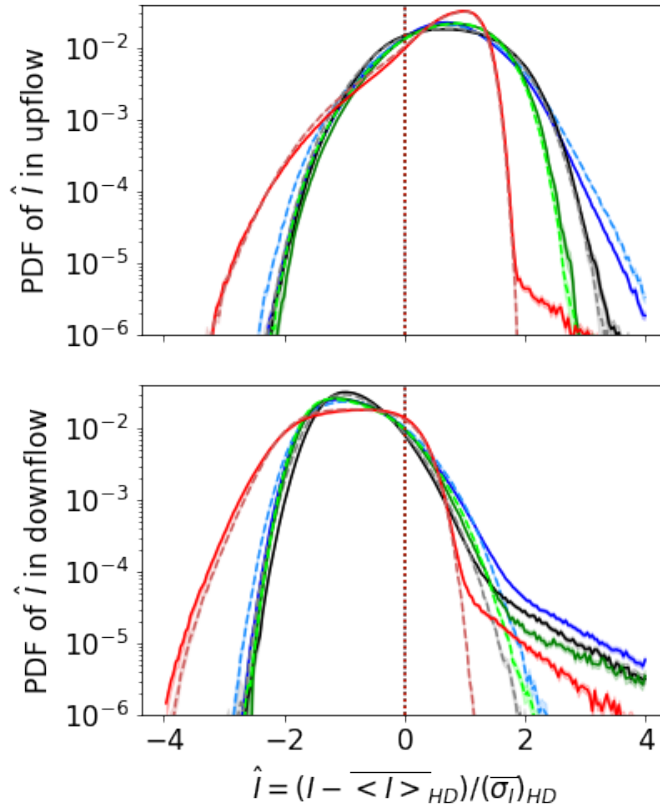

Figure 3.5: PDF of the normalized intensity $\hat{I} = (I - \overline{\langle I \rangle_{\mathrm{HD}}})/\overline{\sigma_{I_{\mathrm{HD}}}}$ for the SSD (*solid*) and HD (*dashed*) cases in upflows (*top*) and downflows *bottom*

In Fig. 3.5, we plot the PDF of the normalized intensity $\hat{I} = (I - \langle \bar{I}_{\mathrm{HD}} \rangle)/\langle \sigma_{I_{\mathrm{HD}}} \rangle$ in upflows and downflows. This form of normalization allows us to account for the significant change in contrast $c = \overline{\sigma_I}/\langle I \rangle$ (see Table 3.2 for individual values of $I_{\mathrm{bol}}, \sigma_I$ and c) between the stellar types while comparing shape of the PDFs, as well as properly compare the change in PDFs between the SSD and the HD case.
Both upflows and downflows show peaked distributions, with a narrow bright peak for up-

flows and a broad dark peak for downflows. This is consistent with distributions obtained from a variety of other simulations o stellar photospheres (Magic et al. 2013, Beeck et al. 2013a, Salhab et al. 2018, Beeck et al. 2012). The bright tail for the upflow distribution shows an inverse trend in slope with T_{eff}, with M-star having an almost vertical tail. This probably reflects the difference in spread in intensities with T_{eff} (see column 5 of Table 3.2). Upflows for G-,K- and M-star show an enhancement in bright tail for SSD cases. However, the F-star has the opposite trend. In addition, all downflow distributions exhibit a bright tail for the SSD cases. This corresponds to formation of bright points in the intergranular lanes.
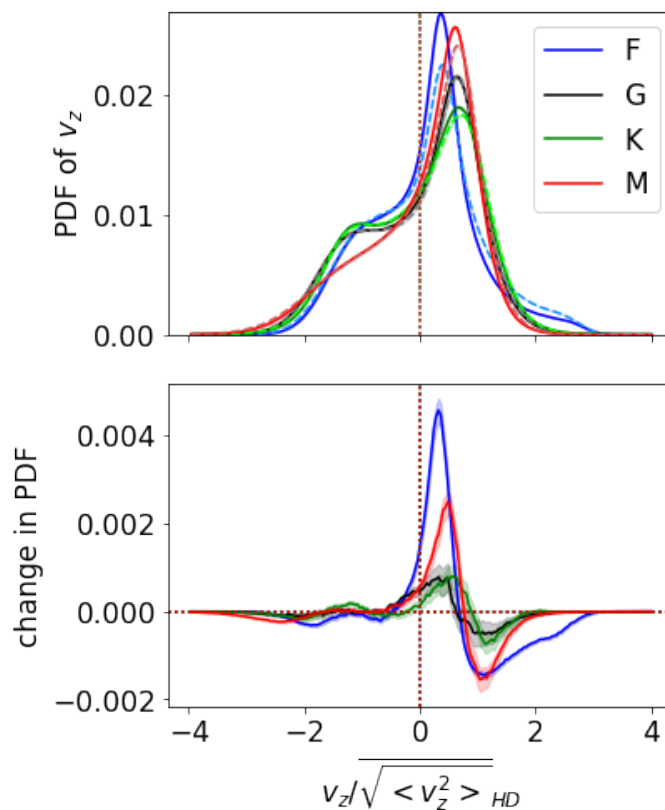
3.3.3 Vertical velocity

Figure 3.6: Vertical velocity v_z normalized by the r.m.s vertical velocity in the HD case $(v_{z,rms})_{HD}$. *Top*: PDF of $v_z/(v_{z,rms})_{HD}$ for the SSD (*solid*) as well as HD (*dashed*) cases. *Bottom*: The difference between the PDF for SSD and HD cases $v_{z,SSD} - v_{z,HD}$.

In Paper 1, we showed that there is a general reduction in vertical velocity v_z for SSD cases near the photosphere. Here we examine, in detail, how the distribution of v_z changes relative to the HD cases when accounting for the magnetic field generation.

The top panel of Fig. 3.6 shows the PDF of v_z at the $\tau = 1$ iso-surface, normalized by $(v_{z,rms})_{HD}$. As with intensity, this normalization allows us to compare the shapes of the PDF between the different stars and to examine the changes between the SSD and HD cases (Fig. 3.6, bottom panel). First of all, we note that all cases show a similar PDF,

with a sharp high peak for upflows and a broad low peak for downflows. There are a couple of exceptions to the general trend: the downflow peak for the M-star is lower than for the others. This might partly be a consequence of a somewhat higher upflow fraction for the M-star (~60%) compared to the other stars (~57-58%). Another difference is the upflow peak for the F-star, which is offset to relatively smaller velocities compared to the other stellar types. This is consistent with a relatively thicker tail for the high upflow velocities v_z, and probably reflects the larger spread in v_z for the F-star. Nevertheless, the distribution of velocities is remarkably similar.

With the introduction of SSD magnetic fields, we see that there is a decrease in the mean upflow velocities. The mean downflow velocities remain relatively unchanged, perhaps because most downflows are probably along vertical magnetic fields in the downflow lanes and the flow there is relatively unhindered.

3.3.4   Spatial distribution of energy

The spatial power spectra plot for the magnetic energy (ME) in Fig. 3.7 (top panel) shows a fairly similar distribution for the G, K and M-star, whereas for the F-star, the spectra is a slightly steeper at the larger scales and has higher power than the spectra for other stars at all wavenumbers. The power spectra for kinetic energy (KE) (middle panel) are also very similar for all the stars at smaller wavenumbers and roughly similar for the larger wavenumbers. In fact, the relative changes in the KE power spectra between the SSD and the HD cases (bottom panel) are remarkably similar for all cases, with a decrease in energy at the largest scales (smallest wavenumbers) and the smallest scales (largest wave numbers). On the other hand, there is no significant change in the power at scales roughly corresponding to granule sizes (see Sect. 3.3.2 for details on granulation scales). Since the dimensions of all the stars are scaled to have similar number of vertical pressure scale heights (and the horizontal size is scaled accordingly to maintain aspect ratio), the similarity in all the power spectra point to a simple pressure scale height scaling of the relevant dynamics. Energy for the magnetic fields is extracted from the KE reservoir at small (subgranular) scales, which leads to near-equipartition fields, and this ME cascades to the largest scales, resulting in a net reduction of average KE.

3.4   Discussion

3.4.1   Magnetic fields and convective collapse

As mentioned in the introduction, the distribution of the magnitude of small-scale magnetic fields is well-studied for the solar case. The weak (sub-kG) field distribution is explained in terms of an equipartition between KE and ME: weak turbulent magnetic fields get carried upward and outwards from granule centers and get collected in intergranular lanes up to kinetic energy equipartition in a process called flux expulsion (Weiss 1966). However, the field strength corresponding to KE equipartition is substantially sub-kG. To explain the presence of kG fields, the convective collapse mechanism (Spruit and Zweibel 1979, Spruit 1979) is usually invoked. The process can be understood as follows: a substantial amount of magnetic field collects in an intergranular lane and starts
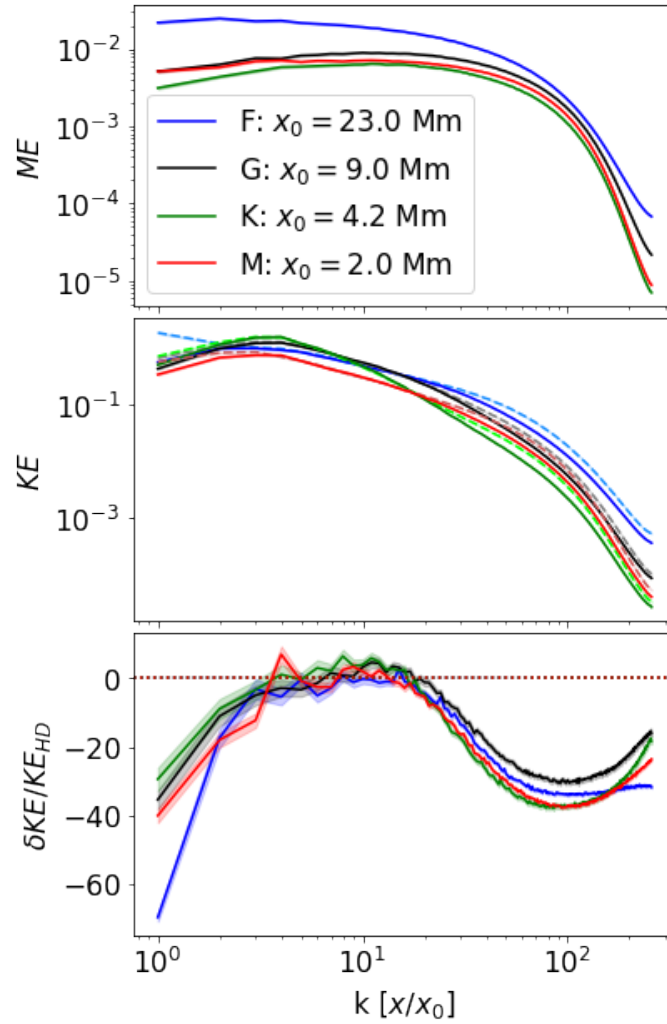
Figure 3.7: Spatial powerspectra of magnetic and kinetic energies. *Top*: Power spectrum of magnetic energy for all the SSD cases. *Middle*: Power spectrum of the kinetic energy for all the SSD (*solid, dark*) and HD (*dashed, light*) cases. *Bottom*: Percent change in the kinetic energy power spectrum for SSD cases, relative to HD cases. The top and middle plots are normalized by the total kinetic energy for the F-star (*solid blue*).

forming a nascent flux tube. For the tube to persist, there has to be pressure balance in the horizontal direction. Due to presence of magnetic fields, the plasma in the flux tube also has a magnetic pressure $B^2/8\pi$. To account for this, the gas pressure p_{gas} within the tube has to be lower than surrounding plasma pressure. Assuming horizontal temperature equilibrium, this implies a reduction in density, giving rise to a plasma instability. For the case of downward[2] displacement, the flux tube gets squeezed horizontally till a new equilibrium state is achieved with stronger field strength. Spruit (1979) showed that the instability can occur for an initial plasma $\beta = 8\pi p_{gas}/B^2$ between 2 and 6.7 within the flux tube. Stronger fields ($\beta < 2$) are stable on their own and weaker fields ($\beta > 6.7$) don't

---

[2]The case of upward motion of plasma causes the magnetic field to expand outwards and eventually results in normal convection (Spruit 1979).

persist long enough to form flux concentrations.

The minimum β for which the convective collapse mechanism can function gives a sort of efficiency of the mechanism. Rajaguru et al. (2002) used this idea and solved the linear eigenvalue problem in Spruit and Zweibel (1979) for different stellar types to obtain a set of minimum β. The values (tabulated in Table 2 of their paper) show a trend of increasing efficiency with increasing T_{eff} and decreasing g. This would imply that the convective collapse mechanism is more efficient in hotter stars and can lead to stronger fields relative to pressure equipartition.

The convective collapse mechanism allows, in principle, intensification of magnetic field up to gas pressure equipartition with the surroundings, that is $B_{\text{eqp}} = \sqrt{8\pi p_{\text{gas}}}$. For the sun, this would be around 1.8 kG in the photosphere. However, intensification beyond B_{eqp} requires consideration of other factors like magnetic tension and turbulent pressure. Some idealized convection studies have indeed shown to result in magnetic field concentrations well above B_{eqp}, for example, in Bushby et al. (2008), where they cite dynamical[3] pressure as a major factor leading to super equipartition fields. As discussed in Paper I, turbulent pressure becomes more important for hotter stars in force balance, especially near the surface, which could explain field strengths greater than B_{eqp}. In addition, magnetic tension within the flux tube due to horizontal fields could also reduce the force required to balance against external pressure, allowing stronger field concentrations in the vertical direction.

3.4.2   Energy distribution and convective blueshift

Table 3.4: Change in proxy convective blueshift v_b

Simulation	$v_{b,\text{SSD}}$ (m/s)	$v_{b,\text{HD}}$ (m/s)	δv_b (m/s)
F3V	1091 ± 10	1395 ± 14	-304 ± 17
G2V	287.0 ± 8.6	310.0 ± 12.9	-23.0 ± 15.5
K0V	140.1 ± 3.8	142.3 ± 3.5	-2.2 ± 5.1
M0V	18.2 ± 1.7	20.7 ± 2.4	-2.5 ± 2.9

Our simulations show that the presence of SSD fields results in reduction of KE at sub-granular scales as well as the scale of the whole box. However, at the scales associated with granule size, there doesn't seem to be any significant change. The change at the largest scales is just a reflection of the overall reduction in convective velocities for the SSD case as ME cascades to the largest scales. An observational signature associated with this reduction is the convective blueshift of photospheric lines (Dravins et al. 1981). Convective blueshift is one of the few measurable quantities that encodes information about stellar granulation. Since these simulations are gray, we cannot calculate line bisectors, etc. Hence, we calculate a proxy convective blueshift v_b based on bolometric intensity. We define this as:

$$v_b = \left(\sum_{x,y} (v_z)_{x,y} (I_{\text{bol}})_{x,y} \right) / \left(\sum_{x,y} (I_{\text{bol}})_{x,y} \right) \tag{3.1}$$

---

[3]The dynamical pressure as described in Bushby et al. (2008) is the same as the definition of turbulent pressure as considered in Appendix B of Paper 1, that is, the contribution to force balance from Reynolds and Maxwell stresses arising from plasma motions against a stationary background.

Here, v_z is the vertical velocity for the $\tau = 1$ iso-surface and the x, y subscript refers to the fact the sum is computed for each pixel on the surface. In Table 3.4, the average v_b for F-star decreases by ~ 300 m/s in the presence of SSD fields. The G-star also shows a change of ~ 20 m/s, but it is close to the standard error (as defined in Sect. 3.2) of ~ 15 m/s. For the K and the M-star the change in v_b is negligible compared to the standard error. We note that this is just an indicator of expected blueshift for photospheric lines and a more rigorous analysis would involve synthesizing spectral lines from non-grey runs and computing, e.g, line bisectors.

The reduction of KE at smallest scales of around 40% (see Fig. 3.7 bottom panel near $k{\sim}10^2$) reflects the near-equipartition division of energy between KE and ME at the scales where field amplification takes place. Most of this field is produced from the turbulent upflows in granules, and subsequently gets concentrated in downflow lanes. This has been extensively studied for the solar case as well as shown to be quite universal in mechanism and energy transfer properties regardless of the physical setup (Moll et al. 2011). This is consistent with the similar distributions of energies for all stellar types discussed here.

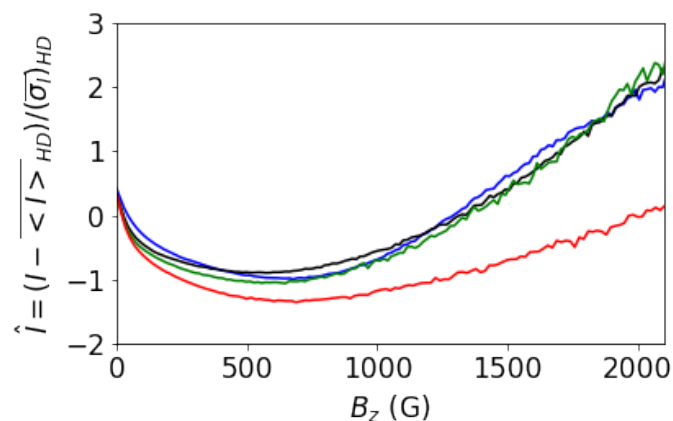### 3.4.3 Granulation and intensity distribution

Figure 3.8: Normalized intensity averaged over each B_z bin on the horizontal axis

All models show slight changes in the apparent granulation with the inclusion of SSD fields. In Paper I, we showed that the inclusion of SSD fields results in a reduction in the ratio of horizontal to vertical velocities $v_{h,\mathrm{rms}}/v_{z,\mathrm{rms}}$ as well as the density scale height H_ρ. Since, based on simple momentum conservation arguments, the granule diameter is given by $D \approx 4(v_h/v_z)H_\rho$ (Nordlund et al. 2009), one would expect the granule size to decrease accordingly. To check that, we base the average granule size on the peak of the spatial powerspectrum P_k of I_{bol}. Previous simulations have shown a tight correlation between granule diameters derived from this relation and P_k (Magic et al. 2013). A decrease in granule size would imply a shift to smaller spatial scales (higher spatial frequency) of the peak. This is, in fact, the case for all the stars, as shown in Table 3.3. This is also supported by observational indications of the relation between magnetic field and granule size for the Sun. Studies of variation in granule size within an active region using SST/CRISP data (Narayan and Scharmer 2010) and over solar activity using SDO/HMI data (Ballot

et al. 2021), show a general inverse correlation between the granule size and the magnetic field strength.

At the smaller scales, the features are more varied between spectral types. As mentioned before, all cases exhibit magnetic bright points in intergranular lanes which are well-correlated with magnetic field concentrations as shown in Fig. 3.8 (but not so strongly for the M-star). However, there are differences in where the $\tau = 1$ surface is formed with respect to where the energy transfer shifts from convective to radiative (Nordlund and Dravins 1990). As discussed in Sect. 4.2 of Paper I, for the F and G-star, the $\tau = 1$ layer forms below where most of overturning of plasma takes place, leading to naked granules whereas for the K and M-star, it forms above, leading to hidden granules (see also Sect. 3.2 of Beeck et al. (2013b) for a more comprehensive description of what constitutes a naked vs. hidden granule). Especially for the F-star, we see turbulent substructure in granulation very clearly in the HD case. However, with SSD fields, this substructure smooths out significantly as the magnetic field ends up acting like an effective viscosity hindering the flow. This affects not only the intensity distribution but also the overall radiative flux: For the F-star, there is a slight decrease in the bolometric intensity (see column 4 of Table 3.2). This effect is not so strong for the G and K star, and there is a slight increase in bolometric intensity due to presence of bright points. For the M-star, there is practically no change as bright points are relatively infrequent.

3.5 Conclusion

The presence of SSD fields in our simulations affects the photosphere in a rather similar manner for the cool-star spectral types considered here: fields are amplified due to turbulent plasma motions (mostly due to the shearing motion between upflows and downflow lanes, see Kitiashvili et al. (2015)). These fields then get collected in intergranular lanes, where they get concentrated to kG levels by convective collapse to roughly equipartition levels with gas pressure. Magnetic bright points are also ubiquitous in the downflow lanes, with a clear signature in the intensity distribution and a mild trend in distribution with T_{eff}. There is also an overall slight decrease in granule size. Because of the SSD fields, the upflow velocities also decrease, again with a similar signature in PDFs of v_z for all cases. This decrease in upflow velocities signals a possible reduction in expected convective blueshift. In absence of spectral lines, a proxy convective blueshift is computed which is lower in magnitude for the SSD cases compared to the HD cases, with the difference scaling with T_{eff}. The decrease in proxy convective blueshift could imply an effect on spectral line shifts, limb darkening as well as stellar variability at short time scales. We plan to investigate these possibilities in a subsequent paper in this series.

4 Conclusion and outlook

Our simulations represent the first models of stellar convection with an self-consistently generated magnetic fields via an SSD mechanism. Four cool main sequence stars (F3V, G2V, K0V and M0V) are considered in this work. The energy contained in these fields is extracted mainly from the kinetic plasma motions, and is within an order of magnitude of the kinetic energy throughout the box. Beneath the surface, the major change with respect to hydrodynamic simulations is a reduction in convective velocities, and accordingly, turbulent pressure, for all cases. The magnitude of this change scales directly with effective temperature. A change in turbulent pressure implies a change in density scale height. For the F-star in particular, this effect is strong enough to change the background stratification in density and gas pressure by around a percent or so near the surface.

At the optical surface itself, the distribution of magnetic fields is very similar between all the cases, with an average photospheric field strength between 100 to 200 G (180 G for the F-star, 120 G for the G star and 100 G for K- and M-star). The fraction of kilogauss fields is also very similar, ranging from 0.4% to 0.8%. The presence of these fields results in appearance of bright points in intergranular lanes as well as a slight reduction in the spatial extent of granules due to the smaller density scale height. The spatial distribution of magnetic and kinetic energies is also quite similar, implying a simple pressure scale height scaling of the dynamics between the simulations. The SSD runs also exhibit a reduction in the upflow velocities, which could affect convective blueshift of photospheric spectral lines.

In our simulations we see small but significant changes in the intensity characteristics due to SSD fields. It is possible that these changes could affect theoretical limb darkening profiles. The associated changes in granulation could also influence aspects of stellar variability, e.g., p-mode oscillation frequencies. The upcoming ESA's PLATO mission will have unprecedented accuracy in stellar photometry, allowing detection and characterization of transiting rocky exoplanets. In addition, the wealth of asteroseismic data will allow precise determination of stellar ages and interiors. Selected targets will be considered for RV measurements via space (JWST) and ground based (ESPRESSO-VLT) spectrometry, allowing characterization of exoplanetary atmospheres. Understanding the contribution of stellar "noise" to lightcurves is, therefore, essential for minimizing the error in these detections. With these factors in mind, it becomes imperative that accurate 3D models of stellar atmospheres be used for synthetic spectra. The work presented in this thesis is but a starting point for modelling stellar atmospheres with self-consistently generated quiet star magnetic fields. This work, along with the work on investigating the effect of SSD fields on stars with different metallicities with other co-authors lays the foundation for constructing a grid of such stellar atmospheres with SSD fields. Comparable to purely hydrodynamic grids like STAGGER and CIFIST, this will cover a range in effective tem-

peratures, surface gravities and metallicities.

There are a number of applications for such a grid. The synthetic spectra generated from 3D models of the STAGGER grid already show a systematic difference in bolometric corrections for various commonly used bands compared to 1D models (Chiavassa et al. 2018). Our models also show slight changes in effective temperatures derived from angle-averaged bolometric intensity, which could influence synthetic colors in various bandpasses. Better models should improve determination of effective temperatures. In addition, precise measurement of shifts in spectral lines are important for wavelength calibration in RV measurements. Spectral lines generated from 3D atmospheres show the effect of convection on line profiles and lead to curved C-shape (and sometimes, inverse-C shaped) line bisectors. These atmospheres have already been used for reducing RV measurement uncertainties (Zwitter et al. 2021). Since our hotter simulations show changes in convective velocity and a very simple proxy convective blueshift based on bolometric intensity, we believe the spectra generated from our models would allow synthesis of more accurate spectral line profiles, which will become important for extremely high resolution RV measurements (approaching cm/s precision range) using instruments like ESPRESSO.

For future investigations, we plan to run these simulations with non-grey radiative transfer allowing a more accurate modelling of the dynamics in and above the photosphere. From an observational perspective, synthetic spectra and colors will be computed to investigate limb darkening and convective blueshift as well as stellar variability due to granulation. This will provide more accurate stellar atmosphere for modelling exoplanetary transists as well as the possibility of constraining stellar abundances more precisely.

Bibliography

Allard, F., Hauschildt, P. H., 1995, Model Atmospheres for M (Sub)Dwarf Stars. I. The Base Model Grid, ApJ, 445, 433, `astro-ph/9601150`

Asplund, M., Nordlund, Å., Trampedach, R., Allende Prieto, C., Stein, R. F., 2000, Line formation in solar granulation. I. Fe line shapes, shifts and asymmetries, A&A, 359, 729–742, `astro-ph/0005320`

Asplund, M., Grevesse, N., Sauval, A. J., Scott, P., 2009, The Chemical Composition of the Sun, ARA&A, 47, 481–522, `0909.0948`

Asplund, M., Amarsi, A. M., Grevesse, N., 2021, The chemical make-up of the Sun: A 2020 vision, A&A, 653, A141, `2105.01661`

Babcock, H. W., 1947, Zeeman Effect in Stellar Spectra., ApJ, 105, 105

Babcock, H. W., 1961, The Topology of the Sun's Magnetic Field and the 22-YEAR Cycle., ApJ, 133, 572

Baliunas, S. L., Donahue, R. A., Soon, W. H., Horne, J. H., Frazer, J., Woodard-Eklund, L., Bradford, M., Rao, L. M., Wilson, O. C., Zhang, Q., Bennett, W., Briggs, J., Carroll, S. M., Duncan, D. K., Figueroa, D., Lanning, H. H., Misch, T., Mueller, J., Noyes, R. W., Poppe, D., Porter, A. C., Robinson, C. R., Russell, J., Shelton, J. C., Soyumer, T., Vaughan, A. H., Whitney, J. H., 1995, Chromospheric Variations in Main-Sequence Stars. II., ApJ, 438, 269

Ballot, J., Roudier, T., Malherbe, J. M., Frank, Z., 2021, Changes in granulation scales over the solar cycle seen with SDO/HMI and Hinode/SOT, arXiv e-prints, arXiv:2106.03556, `2106.03556`

Barnes, S. A., 2003, On the Rotational Evolution of Solar- and Late-Type Stars, Its Magnetic Origins, and the Possibility of Stellar Gyrochronology, ApJ, 586, 464–479, `astro-ph/0303631`

Bastien, F. A., Stassun, K. G., Basri, G., Pepper, J., 2013, An observational correlation between stellar brightness variations and surface gravity, Nature, 500, 427–430, `1308.4728`

Bastien, F. A., Stassun, K. G., Basri, G., Pepper, J., 2016, A Granulation "Flicker"-based Measure of Stellar Surface Gravity, ApJ, 818, 43, `1512.03454`

Beeck, B., Collet, R., Steffen, M., Asplund, M., Cameron, R. H., Freytag, B., Hayek, W., Ludwig, H. G., Schüssler, M., 2012, Simulations of the solar near-surface layers with the CO5BOLD, MURaM, and Stagger codes, A&A, 539, A121, `1201.1103`

Beeck, B., Cameron, R. H., Reiners, A., Schüssler, M., 2013a, Three-dimensional simulations of near-surface convection in main-sequence stars. I. Overall structure, A&A, 558, A48, `1308.4874`

Beeck, B., Cameron, R. H., Reiners, A., Schüssler, M., 2013b, Three-dimensional simulations of near-surface convection in main-sequence stars. II. Properties of granulation and spectral lines, A&A, 558, A49, `1308.4873`

Beeck, B., Schüssler, M., Cameron, R. H., Reiners, A., 2015a, Three-dimensional simulations of near-surface convection in main-sequence stars. III. The structure of small-scale magnetic flux concentrations, A&A, 581, A42, `1505.04739`

Beeck, B., Schüssler, M., Cameron, R. H., Reiners, A., 2015b, Three-dimensional simulations of near-surface convection in main-sequence stars. III. The structure of small-scale magnetic flux concentrations, A&A, 581, A42, `1505.04739`

Bellot Rubio, L., Orozco Suárez, D., 2019, Quiet Sun magnetic fields: an observational view, Living Reviews in Solar Physics, 16, 1

Bercik, D. J., Fisher, G. H., Johns-Krull, C. M., Abbett, W. P., 2005, Convective Dynamos and the Minimum X-Ray Flux in Main-Sequence Stars, ApJ, 631, 529–539, `astro-ph/0506027`

Bhatia, T. S., Cameron, R. H., Solanki, S. K., Peter, H., Przybylski, D., Witzke, V., Shapiro, A., 2022, Small-scale dynamo in cool stars. I. Changes in stratification and near-surface convection for main-sequence spectral types, A&A, 663, A166, `2206.00064`

Blandford, R. D., Znajek, R. L., 1977, Electromagnetic extraction of energy from Kerr black holes., MNRAS, 179, 433–456

Böhm-Vitense, E., 1958, Über die Wasserstoffkonvektionszone in Sternen verschiedener Effektivtemperaturen und Leuchtkräfte. Mit 5 Textabbildungen, ZfA, 46, 108

Boris, J. P., 1970, A physically motivated solution of the alfvén problem, NRL Memorandum Report 2167

Borucki, W. J., Koch, D., Basri, G., Batalha, N., Brown, T., Caldwell, D., Caldwell, J., Christensen-Dalsgaard, J., Cochran, W. D., DeVore, E., Dunham, E. W., Dupree, A. K., Gautier, T. N., Geary, J. C., Gilliland, R., Gould, A., Howell, S. B., Jenkins, J. M., Kondo, Y., Latham, D. W., Marcy, G. W., Meibom, S., Kjeldsen, H., Lissauer, J. J., Monet, D. G., Morrison, D., Sasselov, D., Tarter, J., Boss, A., Brownlee, D., Owen, T., Buzasi, D., Charbonneau, D., Doyle, L., Fortney, J., Ford, E. B., Holman, M. J., Seager, S., Steffen, J. H., Welsh, W. F., Rowe, J., Anderson, H., Buchhave, L., Ciardi, D., Walkowicz, L., Sherry, W., Horch, E., Isaacson, H., Everett, M. E., Fischer, D., Torres, G., Johnson, J. A., Endl, M., MacQueen, P., Bryson, S. T., Dotson, J., Haas,

M., Kolodziejczak, J., Van Cleve, J., Chandrasekaran, H., Twicken, J. D., Quintana, E. V., Clarke, B. D., Allen, C., Li, J., Wu, H., Tenenbaum, P., Verner, E., Bruhweiler, F., Barnes, J., Prsa, A., 2010, Kepler Planet-Detection Mission: Introduction and First Results, Science, 327, 977

Brandenburg, A., Subramanian, K., 2005a, Astrophysical magnetic fields and nonlinear dynamo theory, Phys. Rep., 417, 1–209, `astro-ph/0405052`

Brandenburg, A., Subramanian, K., 2005b, Astrophysical magnetic fields and nonlinear dynamo theory, Phys. Rep., 417, 1–209, `astro-ph/0405052`

Brun, A. S., Browning, M. K., 2017, Magnetism, dynamo action and the solar-stellar connection, Living Reviews in Solar Physics, 14, 4

Buehler, D., Lagg, A., Solanki, S. K., 2013, Quiet Sun magnetic fields observed by Hinode: Support for a local dynamo, A&A, 555, A33, `1307.0789`

Bushby, P. J., Houghton, S. M., Proctor, M. R. E., Weiss, N. O., 2008, Convective intensification of magnetic fields in the quiet Sun, MNRAS, 387, 698–706, `0804.1238`

Carbon, D. F., Gingerich, O., 1969, The Grid of Model Stellar Atmospheres from 4000° to 10,000°, in Theory and Observation of Normal Stellar Atmospheres, (Ed.) O. Gingerich, p. 377

Castelli, F., Kurucz, R. L., 2003, New Grids of ATLAS9 Model Atmospheres, in Modelling of Stellar Atmospheres, (Eds.) N. Piskunov, W. W. Weiss, D. F. Gray, vol. 210, p. A20, `astro-ph/0405087`

Cattaneo, F., 1999, On the Origin of Magnetic Fields in the Quiet Photosphere, ApJ, 515, L39–L42

Charbonneau, P., 2014, Solar Dynamo Theory, ARA&A, 52, 251–290

Chiavassa, A., Casagrande, L., Collet, R., Magic, Z., Bigot, L., Thévenin, F., Asplund, M., 2018, The STAGGER-grid: A grid of 3D stellar atmosphere models. V. Synthetic stellar spectra and broad-band photometry, A&A, 611, A11, `1801.01895`

Christensen-Dalsgaard, J., Dappen, W., Ajukov, S. V., Anderson, E. R., Antia, H. M., Basu, S., Baturin, V. A., Berthomieu, G., Chaboyer, B., Chitre, S. M., Cox, A. N., Demarque, P., Donatowicz, J., Dziembowski, W. A., Gabriel, M., Gough, D. O., Guenther, D. B., Guzik, J. A., Harvey, J. W., Hill, F., Houdek, G., Iglesias, C. A., Kosovichev, A. G., Leibacher, J. W., Morel, P., Proffitt, C. R., Provost, J., Reiter, J., Rhodes, E. J., J., Rogers, F. J., Roxburgh, I. W., Thompson, M. J., Ulrich, R. K., 1996, The Current State of Solar Modeling, Science, 272, 1286–1292

Crass, J., Gaudi, B. S., Leifer, S., Beichman, C., Bender, C., Blackwood, G., Burt, J. A., Callas, J. L., Cegla, H. M., Diddams, S. A., Dumusque, X., Eastman, J. D., Ford, E. B., Fulton, B., Gibson, R., Halverson, S., Haywood, R. D., Hearty, F., Howard, A. W., Latham, D. W., Löhner-Böttcher, J., Mamajek, E. E., Mortier, A., Newman, P., Plavchan, P., Quirrenbach, A., Reiners, A., Robertson, P., Roy, A., Schwab, C.,

Seifahrt, A., Szentgyorgyi, A., Terrien, R., Teske, J. K., Thompson, S., Vasisht, G., 2021, Extreme Precision Radial Velocity Working Group Final Report, arXiv e-prints, arXiv:2107.14291, `2107.14291`

Danilovic, S., Schüssler, M., Solanki, S. K., 2010, Probing quiet Sun magnetism using MURaM simulations and Hinode/SP results: support for a local dynamo, A&A, 513, A1, `1001.2183`

Das, U., Mukhopadhyay, B., 2013, New mass limit for white dwarfs: Super-chandrasekhar type ia supernova as a new standard candle, Phys. Rev. Lett., 110, 071 102

de Wijn, A. G., Stenflo, J. O., Solanki, S. K., Tsuneta, S., 2009, Small-Scale Solar Magnetic Fields, Space Sci. Rev., 144, 275–315, `0812.4465`

Dedner, A., Kemm, F., Kröner, D., Munz, C. D., Schnitzer, T., Wesenberg, M., 2002, Hyperbolic Divergence Cleaning for the MHD Equations, Journal of Computational Physics, 175, 645–673

Donati, J. F., Landstreet, J. D., 2009, Magnetic Fields of Nondegenerate Stars, ARA&A, 47, 333–370, `0904.1938`

Donati, J. F., Semel, M., Carter, B. D., Rees, D. E., Collier Cameron, A., 1997, Spectropolarimetric observations of active stars, MNRAS, 291, 658–682

Dravins, D., 1987, Stellar granulation. I - The observability of stellar photospheric convection, A&A, 172, 200–224

Dravins, D., Lindegren, L., Nordlund, A., 1981, Solar granulation - Influence of convection on spectral line asymmetries and wavelength shifts, A&A, 96, 345–364

Duncan, R. C., Thompson, C., 1992, Formation of Very Strongly Magnetized Neutron Stars: Implications for Gamma-Ray Bursts, ApJ, 392, L9

Eddington, A. S., 1926, The Internal Constitution of the Stars, Cambridge University Press

Edvardsson, B., Andersen, J., Gustafsson, B., Lambert, D. L., Nissen, P. E., Tomkin, J., 1993, The chemical evolution of the galactic disk. I. Analysis and results., A&A, 500, 391–442

Falkovich, G., 1994, Bottleneck phenomenon in developed turbulence, Physics of Fluids, 6, 1411–1414

Freytag, B., Steffen, M., Ludwig, H. G., Wedemeyer-Böhm, S., Schaffenberger, W., Steiner, O., 2012, Simulations of stellar convection with CO5BOLD, Journal of Computational Physics, 231, 919–959, `1110.6844`

Gombosi, T. I., Tóth, G., De Zeeuw, D. L., Hansen, K. C., Kabin, K., Powell, K. G., 2002, Semirelativistic Magnetohydrodynamics and Physics-Based Convergence Acceleration, Journal of Computational Physics, 177, 176–205

Gustafsson, B., Bell, R. A., Eriksson, K., Nordlund, A., 1975, Reprint of 1975A&A....42..407G. A grid of model atmospheres for metal-deficient giant stars. I., A&A, 500, 67–92

Gustafsson, B., Edvardsson, B., Eriksson, K., Jørgensen, U. G., Nordlund, Å., Plez, B., 2008, A grid of MARCS model atmospheres for late-type stars. I. Methods and general properties, A&A, 486, 951–970, `0805.0554`

Haugen, N. E., Brandenburg, A., Dobler, W., 2004, Simulations of nonhelical hydromagnetic turbulence, Phys. Rev. E, 70, 016308, `astro-ph/0307059`

Hauschildt, P. H., Allard, F., Baron, E., 1999, The NextGen Model Atmosphere Grid for 3000<=T_{eff}<=10,000 K, ApJ, 512, 377–385, `astro-ph/9807286`

Henyey, L., Vardya, M. S., Bodenheimer, P., 1965, Studies in Stellar Evolution. III. The Calculation of Model Envelopes., ApJ, 142, 841

Hotta, H., Kusano, K., 2021, Solar differential rotation reproduced with high-resolution simulation, Nature Astronomy, 5, 1100–1102, `2109.06280`

Hotta, H., Rempel, M., Yokoyama, T., 2015, Efficient Small-scale Dynamo in the Solar Convection Zone, ApJ, 803, 42, `1502.03846`

Hotta, H., Kusano, K., Shimada, R., 2022, Generation mechanism of solar-like differential rotation in high-resolution simulations, arXiv e-prints, arXiv:2202.04183, `2202.04183`

Howell, S. B., Sobeck, C., Haas, M., Still, M., Barclay, T., Mullally, F., Troeltzsch, J., Aigrain, S., Bryson, S. T., Caldwell, D., Chaplin, W. J., Cochran, W. D., Huber, D., Marcy, G. W., Miglio, A., Najita, J. R., Smith, M., Twicken, J. D., Fortney, J. J., 2014, The K2 Mission: Characterization and Early Results, PASP, 126, 398, `1402.5163`

Irwin, A. W., 2012, FreeEOS: Equation of State for stellar interiors calculations, `1211.002`

Iskakov, A. B., Schekochihin, A. A., Cowley, S. C., McWilliams, J. C., Proctor, M. R. E., 2007, Numerical Demonstration of Fluctuation Dynamo at Low Magnetic Prandtl Numbers, Phys. Rev. Lett., 98, 208501, `astro-ph/0702291`

Jofré, P., Heiter, U., Soubiran, C., 2019, Accuracy and Precision of Industrial Stellar Abundances, ARA&A, 57, 571–616, `1811.08041`

Jørgensen, A. C. S., Weiss, A., 2019, Overcoming the structural surface effect with a realistic treatment of turbulent convection in 1D stellar models, MNRAS, 488, 3463–3473, `1907.06039`

Kazantsev, A. P., 1968, Enhancement of a Magnetic Field by a Conducting Fluid, Soviet Journal of Experimental and Theoretical Physics, 26, 1031

Kippenhahn, R., Weigert, A., Weiss, A., 2013, Stellar Structure and Evolution, Springer Berlin, Heidelberg

Kitiashvili, I. N., Kosovichev, A. G., Mansour, N. N., Wray, A. A., 2015, Realistic Modeling of Local Dynamo Processes on the Sun, ApJ, 809, 84, `1506.08924`

Koester, D., Chanmugam, G., 1990, REVIEW: Physics of white dwarf stars, Reports on Progress in Physics, 53, 837–915

Kraichnan, R. H., Nagarajan, S., 1967, Growth of Turbulent Magnetic Fields, Physics of Fluids, 10, 859–870

Kurucz, R. L., 1979, Model atmospheres for G, F, A, B, and O stars., ApJS, 40, 1–340

Kurucz, R. L., 1996, Model Stellar Atmospheres and Real Stellar Atmospheres, in M.A.S.S., Model Atmospheres and Spectrum Synthesis, (Eds.) S. J. Adelman, F. Kupka, W. W. Weiss, vol. 108 of Astronomical Society of the Pacific Conference Series, p. 2

Lites, B. W., Centeno, R., McIntosh, S. W., 2014, The solar cycle dependence of the weak internetwork flux, PASJ, 66, S4

Ludwig, H. G., Kučinskas, A., 2012, Three-dimensional hydrodynamical CO^{5}BOLD model atmospheres of red giant stars. I. Atmospheric structure of a giant located near the RGB tip, A&A, 547, A118, `1211.7304`

Ludwig, H. G., Caffau, E., Steffen, M., Freytag, B., Bonifacio, P., Kučinskas, A., 2009, The CIFIST 3D model atmosphere grid., Mem. SA.It., 80, 711, `0908.4496`

Magic, Z., Collet, R., Asplund, M., Trampedach, R., Hayek, W., Chiavassa, A., Stein, R. F., Nordlund, Å., 2013, The Stagger-grid: A grid of 3D stellar atmosphere models. I. Methods and general properties, A&A, 557, A26, `1302.2621`

Mayor, M., Pepe, F., Queloz, D., Bouchy, F., Rupprecht, G., Lo Curto, G., Avila, G., Benz, W., Bertaux, J. L., Bonfils, X., Dall, T., Dekker, H., Delabre, B., Eckert, W., Fleury, M., Gilliotte, A., Gojak, D., Guzman, J. C., Kohler, D., Lizon, J. L., Longinotti, A., Lovis, C., Megevand, D., Pasquini, L., Reyes, J., Sivan, J. P., Sosnowska, D., Soto, R., Udry, S., van Kesteren, A., Weber, L., Weilenmann, U., 2003, Setting New Standards with HARPS, The Messenger, 114, 20–24

Mestel, L., 1968, Magnetic braking by a stellar wind-I, MNRAS, 138, 359

Moll, R., Pietarila Graham, J., Pratt, J., Cameron, R. H., Müller, W. C., Schüssler, M., 2011, Universality of the Small-scale Dynamo Mechanism, ApJ, 736, 36, `1105.0546`

Narayan, G., Scharmer, G. B., 2010, Small-scale convection signatures associated with a strong plage solar magnetic field, A&A, 524, A3, `1007.4673`

Nordlund, A., 1982, Numerical simulations of the solar granulation. I. Basic equations and methods., A&A, 107, 1–10

Nordlund, A., Dravins, D., 1990, Stellar granulation. III. Hydrodynamic model atmospheres., A&A, 228, 155–183

Nordlund, Å., Stein, R. F., 1990, 3-D simulations of solar and stellar convection and magnetoconvection, Computer Physics Communications, 59, 119–125

Nordlund, A., Spruit, H. C., Ludwig, H. G., Trampedach, R., 1997, Is stellar granulation turbulence?, A&A, 328, 229–234

Nordlund, Å., Stein, R. F., Asplund, M., 2009, Solar Surface Convection, Living Reviews in Solar Physics, 6, 2

Parker, E. N., 1955, Hydromagnetic Dynamo Models., ApJ, 122, 293

Parker, E. N., 1958, Dynamics of the Interplanetary Gas and Magnetic Fields., ApJ, 128, 664

Paxton, B., Smolec, R., Schwab, J., Gautschy, A., Bildsten, L., Cantiello, M., Dotter, A., Farmer, R., Goldberg, J. A., Jermyn, A. S., Kanbur, S. M., Marchant, P., Thoul, A., Townsend, R. H. D., Wolf, W. M., Zhang, M., Timmes, F. X., 2019, Modules for Experiments in Stellar Astrophysics (MESA): Pulsating Variable Stars, Rotation, Convective Boundaries, and Energy Conservation, ApJS, 243, 10, `1903.01426`

Pepe, F., Mayor, M., Queloz, D., Benz, W., Bonfils, X., Bouchy, F., Lo Curto, G., Lovis, C., Mégevand, D., Moutou, C., Naef, D., Rupprecht, G., Santos, N. C., Sivan, J. P., Sosnowska, D., Udry, S., 2004, The HARPS search for southern extra-solar planets. I. HD 330075 b: A new "hot Jupiter", A&A, 423, 385–389, `astro-ph/0405252`

Pepe, F., Cristiani, S., Rebolo, R., Santos, N. C., Dekker, H., Cabral, A., Di Marcantonio, P., Figueira, P., Lo Curto, G., Lovis, C., Mayor, M., Mégevand, D., Molaro, P., Riva, M., Zapatero Osorio, M. R., Amate, M., Manescau, A., Pasquini, L., Zerbi, F. M., Adibekyan, V., Abreu, M., Affolter, M., Alibert, Y., Aliverti, M., Allart, R., Allende Prieto, C., Álvarez, D., Alves, D., Avila, G., Baldini, V., Bandy, T., Barros, S. C. C., Benz, W., Bianco, A., Borsa, F., Bourrier, V., Bouchy, F., Broeg, C., Calderone, G., Cirami, R., Coelho, J., Conconi, P., Coretti, I., Cumani, C., Cupani, G., D'Odorico, V., Damasso, M., Deiries, S., Delabre, B., Demangeon, O. D. S., Dumusque, X., Ehrenreich, D., Faria, J. P., Fragoso, A., Genolet, L., Genoni, M., Génova Santos, R., González Hernández, J. I., Hughes, I., Iwert, O., Kerber, F., Knudstrup, J., Landoni, M., Lavie, B., Lillo-Box, J., Lizon, J. L., Maire, C., Martins, C. J. A. P., Mehner, A., Micela, G., Modigliani, A., Monteiro, M. A., Monteiro, M. J. P. F. G., Moschetti, M., Murphy, M. T., Nunes, N., Oggioni, L., Oliveira, A., Oshagh, M., Pallé, E., Pariani, G., Poretti, E., Rasilla, J. L., Rebordão, J., Redaelli, E. M., Santana Tschudi, S., Santin, P., Santos, P., Ségransan, D., Schmidt, T. M., Segovia, A., Sosnowska, D., Sozzetti, A., Sousa, S. G., Spanò, P., Suárez Mascareño, A., Tabernero, H., Tenegi, F., Udry, S., Zanutta, A., 2021, ESPRESSO at VLT. On-sky performance and first results, A&A, 645, A96, `2010.00316`

Petrovay, K., Szakaly, G., 1993, The origin of intranetwork fields: a small-scale solar dynamo, A&A, 274, 543

Pietarila Graham, J., Cameron, R., Schüssler, M., 2010, Turbulent Small-Scale Dynamo Action in Solar Surface Simulations, ApJ, 714, 1606–1616, `1002.2750`

Przybylski, D., Cameron, R., Solanki, S. K., Rempel, M., Leenaarts, J., Anusha, L. S., Witzke, V., Shapiro, A. I., 2022, Chromospheric Extension of the MURaM Code, arXiv e-prints, arXiv:2204.03126, `2204.03126`

Radick, R. R., Thompson, D. T., Lockwood, G. W., Duncan, D. K., Baggett, W. E., 1987, The Activity, Variability, and Rotation of Lower Main-Sequence Hyades Stars, ApJ, 321, 459

Rajaguru, S. P., Kurucz, R. L., Hasan, S. S., 2002, Convective Intensification of Magnetic Flux Tubes in Stellar Photospheres, ApJ, 565, L101–L104, `astro-ph/0201026`

Rauer, H., Catala, C., Aerts, C., Appourchaux, T., Benz, W., Brandeker, A., Christensen-Dalsgaard, J., Deleuil, M., Gizon, L., Goupil, M. J., Güdel, M., Janot-Pacheco, E., Mas-Hesse, M., Pagano, I., Piotto, G., Pollacco, D., Santos, Ċ., Smith, A., Suárez, J. C., Szabó, R., Udry, S., Adibekyan, V., Alibert, Y., Almenara, J. M., Amaro-Seoane, P., Eiff, M. A.-v., Asplund, M., Antonello, E., Barnes, S., Baudin, F., Belkacem, K., Bergemann, M., Bihain, G., Birch, A. C., Bonfils, X., Boisse, I., Bonomo, A. S., Borsa, F., Brandão, I. M., Brocato, E., Brun, S., Burleigh, M., Burston, R., Cabrera, J., Cassisi, S., Chaplin, W., Charpinet, S., Chiappini, C., Church, R. P., Csizmadia, S., Cunha, M., Damasso, M., Davies, M. B., Deeg, H. J., Díaz, R. F., Dreizler, S., Dreyer, C., Eggenberger, P., Ehrenreich, D., Eigmüller, P., Erikson, A., Farmer, R., Feltzing, S., de Oliveira Fialho, F., Figueira, P., Forveille, T., Fridlund, M., García, R. A., Giommi, P., Giuffrida, G., Godolt, M., Gomes da Silva, J., Granzer, T., Grenfell, J. L., Grotsch-Noels, A., Günther, E., Haswell, C. A., Hatzes, A. P., Hébrard, G., Hekker, S., Helled, R., Heng, K., Jenkins, J. M., Johansen, A., Khodachenko, M. L., Kislyakova, K. G., Kley, W., Kolb, U., Krivova, N., Kupka, F., Lammer, H., Lanza, A. F., Lebreton, Y., Magrin, D., Marcos-Arenal, P., Marrese, P. M., Marques, J. P., Martins, J., Mathis, S., Mathur, S., Messina, S., Miglio, A., Montalban, J., Montalto, M., Monteiro, M. J. P. F. G., Moradi, H., Moravveji, E., Mordasini, C., Morel, T., Mortier, A., Nascimbeni, V., Nelson, R. P., Nielsen, M. B., Noack, L., Norton, A. J., Ofir, A., Oshagh, M., Ouazzani, R. M., Pápics, P., Parro, V. C., Petit, P., Plez, B., Poretti, E., Quirrenbach, A., Ragazzoni, R., Raimondo, G., Rainer, M., Reese, D. R., Redmer, R., Reffert, S., Rojas-Ayala, B., Roxburgh, I. W., Salmon, S., Santerne, A., Schneider, J., Schou, J., Schuh, S., Schunker, H., Silva-Valio, A., Silvotti, R., Skillen, I., Snellen, I., Sohl, F., Sousa, S. G., Sozzetti, A., Stello, D., Strassmeier, K. G., Švanda, M., Szabó, G. M., Tkachenko, A., Valencia, D., Van Grootel, V., Vauclair, S. D., Ventura, P., Wagner, F. W., Walton, N. A., Weingrill, J., Werner, S. C., Wheatley, P. J., Zwintz, K., 2014, The PLATO 2.0 mission, Experimental Astronomy, 38, 249–330, `1310.0696`

Reiners, A., 2012, Observations of Cool-Star Magnetic Fields, Living Reviews in Solar Physics, 9, 1, `1203.0241`

Rempel, M., 2014, Numerical Simulations of Quiet Sun Magnetism: On the Contribution from a Small-scale Dynamo, ApJ, 789, 132, `1405.6814`

Rempel, M., 2017, Extension of the MURaM Radiative MHD Code for Coronal Simulations, ApJ, 834, 10, `1609.09818`

Rempel, M., Schüssler, M., Cameron, R. H., Knölker, M., 2009, Penumbral Structure and Outflows in Simulated Sunspots, Science, 325, 171, `0907.2259`

Ricker, G. R., Winn, J. N., Vanderspek, R., Latham, D. W., Bakos, G. Á., Bean, J. L., Berta-Thompson, Z. K., Brown, T. M., Buchhave, L., Butler, N. R., Butler, R. P., Chaplin, W. J., Charbonneau, D., Christensen-Dalsgaard, J., Clampin, M., Deming, D., Doty, J., De Lee, N., Dressing, C., Dunham, E. W., Endl, M., Fressin, F., Ge, J., Henning, T., Holman, M. J., Howard, A. W., Ida, S., Jenkins, J., Jernigan, G., Johnson, J. A., Kaltenegger, L., Kawai, N., Kjeldsen, H., Laughlin, G., Levine, A. M., Lin, D., Lissauer, J. J., MacQueen, P., Marcy, G., McCullough, P. R., Morton, T. D., Narita, N., Paegert, M., Palle, E., Pepe, F., Pepper, J., Quirrenbach, A., Rinehart, S. A., Sasselov, D., Sato, B., Seager, S., Sozzetti, A., Stassun, K. G., Sullivan, P., Szentgyorgyi, A., Torres, G., Udry, S., Villasenor, J., 2014, Transiting Exoplanet Survey Satellite (TESS), in Space Telescopes and Instrumentation 2014: Optical, Infrared, and Millimeter Wave, (Eds.) J. Oschmann, Jacobus M., M. Clampin, G. G. Fazio, H. A. MacEwen, vol. 9143 of Society of Photo-Optical Instrumentation Engineers (SPIE) Conference Series, p. 914320, `1406.0151`

Rincon, F., 2019, Dynamo theories, Journal of Plasma Physics, 85, 205850401, `1903. 07829`

Roettenbacher, R. M., Monnier, J. D., Korhonen, H., Aarnio, A. N., Baron, F., Che, X., Harmon, R. O., Kővári, Z., Kraus, S., Schaefer, G. H., Torres, G., Zhao, M., Ten Brummelaar, T. A., Sturmann, J., Sturmann, L., 2016, No Sun-like dynamo on the active star ζ Andromedae from starspot asymmetry, Nature, 533, 217–220, `1709.10107`

Salhab, R. G., Steiner, O., Berdyugina, S. V., Freytag, B., Rajaguru, S. P., Steffen, M., 2018, Simulation of the small-scale magnetism in main-sequence stellar atmospheres, A&A, 614, A78

Sánchez Almeida, J., Martínez González, M., 2011, The Magnetic Fields of the Quiet Sun, in Solar Polarization 6, (Eds.) J. R. Kuhn, D. M. Harrington, H. Lin, S. V. Berdyugina, J. Trujillo-Bueno, S. L. Keil, T. Rimmele, vol. 437 of Astronomical Society of the Pacific Conference Series, p. 451, `1105.0387`

Schatzman, E., 1962, A theory of the role of magnetic activity during star formation, Annales d'Astrophysique, 25, 18

Schekochihin, A. A., Cowley, S. C., Maron, J. L., McWilliams, J. C., 2004a, Critical Magnetic Prandtl Number for Small-Scale Dynamo, Phys. Rev. Lett., 92, 054502, `astro-ph/0308336`

Schekochihin, A. A., Cowley, S. C., Taylor, S. F., Maron, J. L., McWilliams, J. C., 2004b, Simulations of the Small-Scale Turbulent Dynamo, ApJ, 612, 276–307, `astro-ph/ 0312046`

Semel, M., 1989, Zeeman-Doppler imaging of active stars. I - Basic principles., A&A, 225, 456–466

Shapiro, A. I., Solanki, S. K., Krivova, N. A., Cameron, R. H., Yeo, K. L., Schmutz, W. K., 2017, The nature of solar brightness variations, Nature Astronomy, 1, 612–616, `1711.04156`

Shchukina, N., Trujillo Bueno, J., 2011, Determining the Magnetization of the Quiet Sun Photosphere from the Hanle Effect and Surface Dynamo Simulations, ApJ, 731, L21, `1103.5652`

Shporer, A., Brown, T., 2011, The Impact of the Convective Blueshift Effect on Spectroscopic Planetary Transits, ApJ, 733, 30, `1103.0775`

Skumanich, A., 1972, Time Scales for Ca II Emission Decay, Rotational Braking, and Lithium Depletion, ApJ, 171, 565

Sneden, C., 1973, The nitrogen abundance of the very metal-poor star HD 122563., ApJ, 184, 839

Solanki, S. K., 1993, Smallscale Solar Magnetic Fields - an Overview, Space Sci. Rev., 63, 1–188

Spruit, H. C., 1976, Pressure equilibrium and energy balance of small photospheric flux-tubes., Sol. Phys., 50, 269–295

Spruit, H. C., 1979, Convective collapse of flux tubes., Sol. Phys., 61, 363–378

Spruit, H. C., 1982, Effect of spots on a star's radius and luminosity, A&A, 108, 348–355

Spruit, H. C., Zweibel, E. G., 1979, Convective instability of thin flux tubes., Sol. Phys., 62, 15–22

Stein, R. F., Nordlund, Å., 1998, Simulations of Solar Granulation. I. General Properties, ApJ, 499, 914–933

Stix, M., 2004, The sun : an introduction, Springer

Strom, S. E., Kurucz, R., 1966, Statistical Procedure for Computing Line-Blanketed Model Stellar Atmospheres., AJ, 71, 181

Trujillo Bueno, J., 2001, Atomic Polarization and the Hanle Effect, in Advanced Solar Polarimetry – Theory, Observation, and Instrumentation, (Ed.) M. Sigwarth, vol. 236 of Astronomical Society of the Pacific Conference Series, p. 161, `astro-ph/0202328`

Trujillo Bueno, J., Shchukina, N., Asensio Ramos, A., 2004, A substantial amount of hidden magnetic energy in the quiet Sun, Nature, 430, 326–329, `astro-ph/0409004`

Vögler, A., Schüssler, M., 2007, A solar surface dynamo, A&A, 465, L43–L46, `astro-ph/0702681`

Vögler, A., Bruls, J. H. M. J., Schüssler, M., 2004, Approximations for non-grey radiative transfer in numerical simulations of the solar photosphere, A&A, 421, 741–754

Vögler, A., Shelyag, S., Schüssler, M., Cattaneo, F., Emonet, T., Linde, T., 2005, Simulations of magneto-convection in the solar photosphere. Equations, methods, and results of the MURaM code, A&A, 429, 335–351

Warnecke, J., Käpylä, Maarit and, G. F., Reinhardt, M., 2022, Numerical evidence for a small-scale dynamo approaching solar magnetic Prandtl numbers, 05 August 2022, PREPRINT (Version 1), Nature Preprint

Weiss, N. O., 1966, The Expulsion of Magnetic Flux by Eddies, Proceedings of the Royal Society of London Series A, 293, 310–328

Wilson, O. C., 1978, Chromospheric variations in main-sequence stars., ApJ, 226, 379–396

Yadav, N., Cameron, R. H., Solanki, S. K., 2021, Vortex flow properties in simulations of solar plage region: Evidence for their role in chromospheric heating, A&A, 645, A3, `2010.14971`

Zwitter, T., Kos, J., Buder, S., Čotar, K., Asplund, M., Bland-Hawthorn, J., Casey, A. R., De Silva, G. M., D'Orazi, V., Freeman, K. C., Hayden, M. R., Lewis, G. F., Lin, J., Lind, K., Martell, S. L., Schlesinger, K. J., Sharma, S., Simpson, J. D., Stello, D., Zucker, D. B., Beeson, K. L., de Grijs, R., Nordlander, T., Ting, Y.-S., Traven, G., Vogrinčič, R., Watson, F., Wittenmyer, R., 2021, The GALAH+ survey: a new library of observed stellar spectra improves radial velocities and hints at motions within M67, MNRAS, 508, 4202–4215, `2012.12201`

Appendix

A   Appendix to chapter 2

A.1   Mach number derivation

We derive the expression for Mach number used in Eq. (2.5) from §2.4.1. Considering the hydrostatic pressure balance equation, the expression for pressure-scale height (H_p), the expression for sound speed (c_s) and the ideal gas equation of state:

$$p' = -g\rho, \tag{A.1}$$
$$H_p = -p/p', \tag{A.2}$$
$$c_s^2 = \gamma p/\rho, \tag{A.3}$$
$$p = \rho(R/\mu)T. \tag{A.4}$$

Here, H_p is the pressure scale height, $p' = dp/dz$, μ is the mean molar mass, and $1/\mu = (1 + E)(X + Y/4 + Z/2)$, where E is ionization fraction and X, Y, Z are the H, He and metal abundances. In the Böhm-Vitense MLT (Böhm-Vitense 1958), convective flux and velocities are expressed as:

$$F_{conv} = \alpha c_p \rho v T(\nabla - \nabla_a)/2, \tag{A.5}$$
$$v^2 = \alpha^2 \delta g H_p (\nabla - \nabla_a)/8. \tag{A.6}$$

Here, α is the mixing length parameter (usually taken to be between 1.5 to 2), $\delta = 1 - (\partial \ln \mu / \partial \ln T)_p$ (abundance gradient with temperature for an ideal gas), $c_p = (\partial U / \partial T)_p + p\delta/(\rho T)$ (heat capacity at constant pressure), and $\nabla = d \ln T / d \ln p$, with the subscript a referring to 'adiabatic.' We refer to chapter 6 of Stix (2004) for more details.

Near the surface, as most energy is carried by radiation, $F_{conv} \approx \sigma T^4$. We take the ratio of Eq. A.5 and Eq. A.6 to eliminate $\nabla - \nabla_a$ and use σT^4 instead of F_{conv}. Taking Mach number $M = v/c_s$ and $c_s = \sqrt{\gamma R T/\mu}$ and eliminating H_p and p using Eq. A.1, A.2, and A.4,

$$M = \left(\frac{\alpha \delta \sigma \mu^{1/2}}{4 c_p \gamma^{3/2} R^{1/2}} \right)^{1/3} T^{5/6} \rho^{-1/3}. \tag{A.7}$$

Using relevant values for the terms in the parentheses (all in cgs), we get Eq. (2.5) in terms of T and ρ as above:
The value of $\mu = 1.2$ assumes $E \sim 0$ near $\tau = 1$. For an M-star, this may not necessarily be the case. However, even if $E \rightarrow 1$, μ changes by a factor of 2 and, accordingly, M changes by a factor of $2^{1/2} \approx 1.4$, and the qualitative result still holds.

$$
\begin{array}{lll}
\alpha & = 1.8 & \text{(average literature value)} \\
\delta & = 1 & \text{(assume } \mu \text{ is constant)} \\
\sigma & = 5.67\text{e-}5 \ \text{erg/cm}^2/\text{s/K}^4 & \text{(Stefan-Boltzmann constant)} \\
\gamma & = 5/3 & \text{(monoatomic adiabatic index)} \\
\mu & = 1.2 & \text{(solar surface abundance)} \\
R & = 8.314\text{e}7 \ \text{erg/K/mol} & \text{(universal gas constant)} \\
c_p & = \gamma R/(\mu(\gamma - 1)) & \text{(isobaric specific heat capacity)}
\end{array}
$$

A.2   Turbulent pressure and pressure scale height derivation

In §2.4.1, the expression used for p_{turb} in Eq. (2.6) can be derived by considering the total (Reynolds and Maxwell) stress tensor, σ_{ij}, for ideal MHD:

$$
\sigma_{ij} = \rho(v_i v_j) + \left(p + \frac{B^2}{8\pi}\right)\delta_{ij} - \frac{B_i B_j}{4\pi}. \tag{A.8}
$$

Here i, j represent the x, y and z directions.

The pressure balance along the vertical (z) direction involves the term $\langle \nabla_z \cdot \sigma_{iz} \rangle_z$ which is equal to $\partial p_{\text{tot}}/\partial z$. We can now compare these two terms to get an expression for total pressure (p_{tot}). Assuming all the off-diagonal terms ($i \neq j$) are negligible (which is akin to saying there is no cross-correlation between the vertical and the horizontal velocity and magnetic field components), we obtain the following:

$$
\langle p_{\text{tot}} \rangle_z = \left\langle \rho v_z^2 + \left(p + \frac{B_x^2 + B_y^2 + B_z^2}{8\pi}\right) - \frac{\left(B_z^2 + \cancelto{0}{B_z B_x} + \cancelto{0}{B_z B_y}\right)}{4\pi}\right\rangle_z, \tag{A.9}
$$

$$
\langle p_{\text{tot}} \rangle_z = \langle \rho v_z^2 \rangle + \langle p \rangle_z + \frac{\langle B_h^2 - B_z^2 \rangle_z}{8\pi}. \tag{A.10}
$$

The next step is to consider how using p_{tot} instead of p affects the density scale height, H_ρ. In Eq. (A.1), we substitute expression for p_{tot}, instead of p, and use Eq. (A.4) to eliminate p. With this, we obtain:

$$
\frac{d}{dz}\left(\rho(RT/\mu + v^2)\right) = -\rho g. \tag{A.11}
$$

Here, we take v^2 to be $v_z^2 + (B_h^2 - B_z^2)/(8\pi\rho)$. Then, the above equation can be rearranged to obtain:

$$
\frac{d\rho}{\rho} = -\frac{g\,dz}{RT/\mu + v^2} - \frac{d(RT/\mu + v^2)}{RT/\mu + v^2}. \tag{A.12}
$$

From this, we can obtain the expression for density scale height, H_ρ, as:

$$
H_\rho = RT/(\mu g) + v^2/g. \tag{A.13}
$$

The second term above includes the contribution from the turbulent pressure. Since this term is almost always smaller for the SSD case relative to the HD case (mainly because the convective velocities are lower for SSD), the corresponding pressure scale height for the SSD cases is also almost always smaller.

A.3   Diagnostics

For any MHD simulation, the computation and evolution of the magnetic field must be divergence free. To ensure this, *MURaM* uses a hyperbolic divB cleaning algorithm (Dedner et al. 2002). Here, we show the horizontally averaged divergence of magnetic field across the box for all four SSD cases. Since the units for $\nabla \cdot B$ are field/length, a proper comparison requires a normalization. We do so with $\|B\|/\Delta z$. As noted in §2.2.2, at best, the error is $O(10^{-3})$.
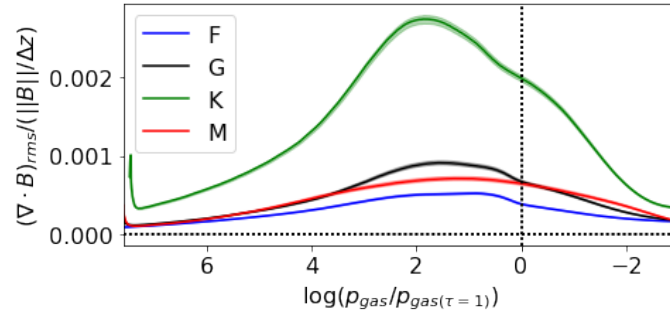

Figure A.1: **div·B** error for the four SSD cases: F, G, K, and M. The quantity plotted is horizontally averaged $(\nabla \cdot \vec{B})_{\mathrm{rms}}/(\|B\|/\Delta z)$.

B Appendix to chapter 3

B.1 Spatial Powerspectrum

To compute the spatial power spectrum, we use the following procedure:

1. Take the 2D FFT of the quantity q (with the zero-frequency mode shifted to the center and higher frequencies going outwards). Depending on the quantity considered, we either take the absolute value of this FFT or multiply it by its the complex conjugate, to get $\tilde{q}$

2. For each radial wave number $k = \sqrt{k_x^2 + k_y^2}$, construct a 1-pixel wide mask (which takes the form of a ring around the center)

3. Take the mean of the absolute value of FFT(I) in each ring and multiply it with the radius of the ring to get the power $P_k = \sum_{\forall x,y \in k} \tilde{q}$

For bolometric intensity, we simply take the absolute value of the power spectrum $\tilde{I_{\mathrm{bol}}} = |\mathrm{FFT}(I_{\mathrm{bol}})|$. For kinetic energy, we multiply FFT($\sqrt{\rho}v$) by its complex conjugate to get $\tilde{\mathrm{KE}} = (\mathrm{FFT}(\sqrt{\rho}v)) \times (\mathrm{FFT}(\sqrt{\rho}v))^*$. For B^2, we do the same

B.2 Additional plots

The distribution of magnetic fields in upflows (Fig. B.2) is remarkably similar for the geometric $\langle \tau \rangle = 1$ slice, whereas for the iso-$\tau = 1$ surface, it shows a clear trend with T_{eff}. In the downflows, however, the trend of kG fields with T_{eff} becomes apparent.
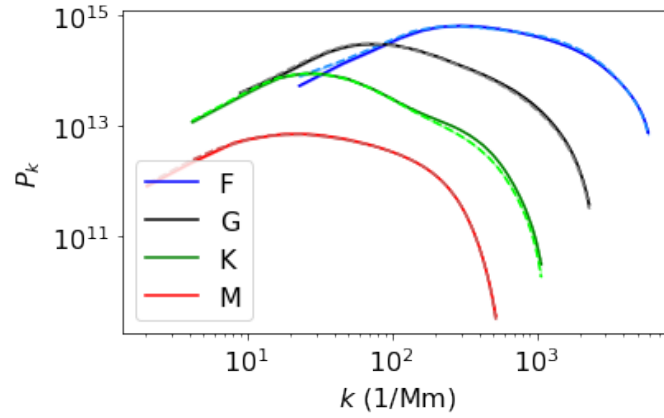
Figure B.1: Spatial power spectra P_k of the bolometric intensity (normalized by total power in SSD F-star case) plotted against spatial frequency $1/x$ in units of Mm^{-1}. Solid (dashed) lines represent the SSD (HD) cases.
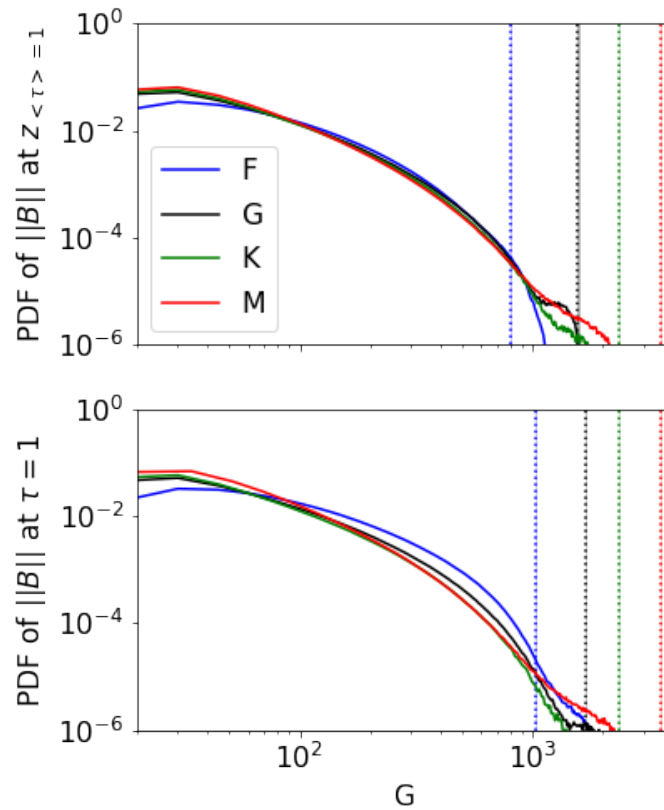

Figure B.2: PDF of the magnitude of magnetic field in upflows, for the geometric surface $z_{\langle\tau\rangle=1}$ (*top*) and for the $\tau = 1$ iso-surface (*bottom*).
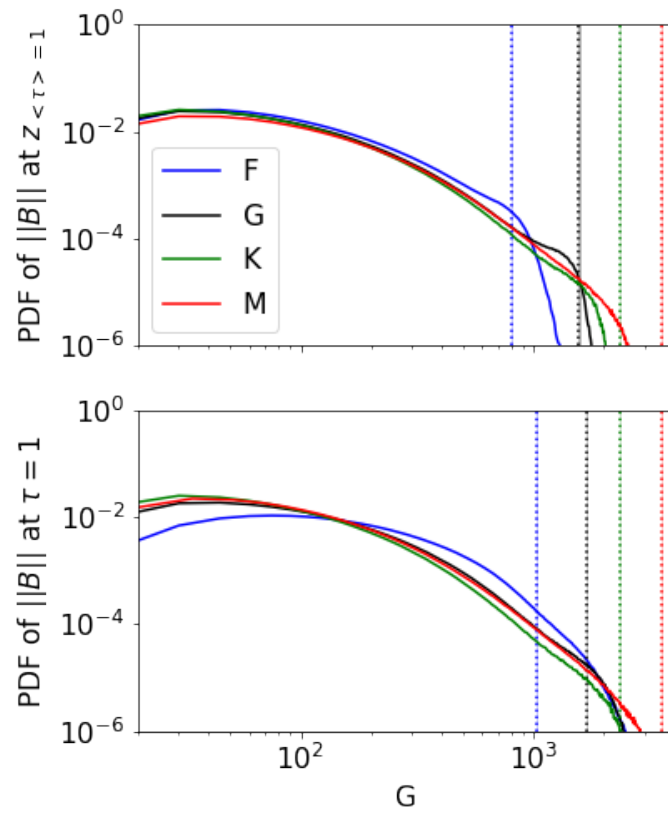
Figure B.3: PDF of the magnitude of magnetic field in downflows, for the geometric surface $z_{\langle\tau\rangle=1}$ (*top*) and for the $\tau = 1$ iso-surface (*bottom*).

Publications

Refereed publications

- **Bhatia, T. S.**, Cameron R. H., Solanki S. K., Peter H., Przybylski D., Witzke V., Shapiro A., 2022, A&A, 663, A166. doi:10.1051/0004-6361/202243607

Conference talks and posters

- Poster - **Bhatia T.**, Cameron R., Solanki S., Peter H., Przybylski D., Witzke V., Shapiro A., 2021, csss.conf, 75. doi:10.5281/zenodo.4562655

- Talk - **Bhatia T.**, Cameron R., Solanki S., Peter H., Przybylski D., Witzke V., Shapiro A., 2021, AAS

- Talk - **Bhatia T. S.**, Cameron R., Solanki S., Peter H., Przbylski D., Witzke V., 2020, SPD

Acknowledgements

I would first like to thank both Robert and Hardi for supervising me throughout this project and dealing with my silly questions, periods of existential doubts and keeping me motivated throughout my PhD. I am aware I have probably not been the easiest person to work with/supervise. I messed more times than it's worth counting, but you both made sure I was on the right track while still letting me figure out and fix my mistakes on my own as much as possible. Thank you for allowing me to learn this. And for almost always eventually being there when I needed you.

I would also like to thank Sami for giving me the opportunity to work on this project, having faith that I was suitable to work on it, and making sure I was always aware of the bigger picture. I would like to thank Sonja for her help with the bureaucratic side of things and for making sure that undergoing the PhD process is somewhat enjoyable under the IMPRS program.

To Damien, thanks for all the (sadistic) bike rides, coffee meets, and all the trash talking to pass time. I thoroughly enjoyed picking your brain while procrastinating on actual work. To Cosima, thanks for all the hikes, rides and movie nights. And for being the first good friend I made here. To Paula, thank you for making sure no matter what was going on in our lives at any point, one Thursday a week, we would run together. And for making sure, sometimes forcefully, that I kept up my running. To Argiris and Dusan, thank you for making office life entertaining, even if it resulted in us "working" only in the loosest sense. To Philipp, thank you for being the first person to actually talk to me properly when I started here, for the good food we cooked and for swims and runs we went on. To Nina, thank you for lots and lots of trash talking, moral support and, of course, bouldering company. To Nils, thank you for shared music tastes and being a good friend. I had a great time during our meals together. To Hanna, thank you for showing kindness to a new PhD student without anywhere to be on his first Christmas eve alone in a foreign country. You are still the nicest person I've got to know here. To Bernhard and the whole DnD group, thank you for making some lockdown evenings bearable. I still await an MS Paint album of our battles. To Jesper, thank you for entertaining conversations, wacky drinking nights and that damn movie. Keep up your zest man, it is rare. To Johannes, for forcing me to be (somewhat) good at bouldering, for weird music tastes and for your terrible sense of humour. To Jonas, for rides, dinners, that one hike (lol) and the best swimming tip I've got from anyone recently. To Jamie, for shared coffee breaks and table tennis matches. To Amanda, for spicy candy and for being a genuinely weird and joyful person. To Patrick, for stupid food challenges and shared misery in dealing with Robert. To all the members of MegaGauss, for helping me stay sane while being able to play (occasionally) good music (we gotta to do a prog rock song at some point!). To Nikolina, Lisa, Juxhin, Simon, Ameya, Rakshit, Isabela, Yara, Felix, Marius, Christian, and so many more that I

interacted with, thank you for making the PhD experience at MPS a fun one.

And of course, I'd like to thank my parents and my brother for their constant support and love. Even when times were tough and unexpected and I was lost, you kept me grounded. Thank you for always being there and inspiring me to work for what I want, stubbornly at times (which reminds me, I still need to force you to sit through long explanations of what I've worked on).

And to my fiancée, Prerna, thank you for giving me some of the best moments of my life. Your faith in me kept me going through the worst of times. I would not be who I am without you. To more time spent living together. Love you, always.

Curriculum vitae

Name: Tanayveer Singh Bhatia
Date of Birth: 17.09.1993
Place of Birth: Ludhiana, India

Education:
April 2019 - Oct 2022
PhD
International Max Planck Research School (IMPRS) at Max Planck Institute for Solar System Research (MPS) and University of Göttingen, Germany

August 2011 - July 2016
Master of Science (M.Sc.) (Integrated) in Physics
Birla Institute of Technology and Science (BITS), Pilani, India
Bachelor of Engineering (B.E.) in Mechanical Engineering
Birla Institute of Technology and Science (BITS), Pilani, India